

Special Section:

Community Earth System
Model High-Resolution
(CESM-HR) Special Collection

Key Points:

- We use spectral methods to examine the role of oceanic and atmospheric processes in Pacific sea surface temperature (SST) and turbulent heat flux variability
- At mid-latitudes, the atmosphere controls variability with scales larger than 2,000 km while ocean processes dominate at smaller scales
- Ocean phenomena drive a red spectrum SST response similar to that induced by the atmosphere, which is mirrored by the turbulent fluxes

Supporting Information:

Supporting Information may be found in the online version of this article.

Correspondence to:

L. C. Laurindo,
laurindo@ucar.edu

Citation:












Laurindo, L. C., Small, R. J., Thompson, L. A., Siqueira, L., Bryan, F. O., Chang, P., et al. (2022). Role of ocean and atmosphere variability in scale-dependent thermodynamic air-sea interactions.

Journal of Geophysical Research: Oceans, 127, e2021JC018340. <https://doi.org/10.1029/2021JC018340>

Received 15 DEC 2021

Accepted 27 JUN 2022

Role of Ocean and Atmosphere Variability in Scale-Dependent Thermodynamic Air-Sea Interactions

Lucas C. Laurindo^{1,2} , R. Justin Small^{1,2} , LuAnne Thompson³ , Leo Siqueira⁴ , Frank O. Bryan² , Ping Chang^{1,5,6} , Gokhan Danabasoglu^{1,2} , Igor V. Kamenkovich⁴ , Ben P. Kirtman⁴ , Hong Wang^{1,7,8} , and Shaoqing Zhang^{1,7,8} 

¹International Laboratory for High-Resolution Earth System Prediction (IHESP), Texas A&M University, College Station, TX, USA, ²National Center for Atmospheric Research, Boulder, CO, USA, ³School of Oceanography, University of Washington, Seattle, WA, USA, ⁴Rosenstiel School of Marine & Atmospheric Science, University of Miami, Miami, FL, USA, ⁵Department of Oceanography, Texas A&M University, College Station, TX, USA, ⁶Department of Atmospheric Sciences, Texas A&M University, College Station, TX, USA, ⁷Laboratory for Ocean Dynamics and Climate, Qingdao Pilot National Laboratory for Marine Science and Technology, Qingdao, China, ⁸Key Laboratory of Physical Oceanography, the College of Oceanic and Atmospheric Sciences, the Institute for Advanced Ocean Study & Center for Deep Ocean Multispheres and Earth System (DOMES), Ocean University of China, Qingdao, China

Abstract This study investigates the influence of oceanic and atmospheric processes in extratropical thermodynamic air-sea interactions resolved by satellite observations (OBS) and by two climate model simulations run with eddy-resolving high-resolution (HR) and eddy-parameterized low-resolution (LR) ocean components. Here, spectral methods are used to characterize the sea surface temperature (SST) and turbulent heat flux (THF) variability and co-variability over scales between 50 and 10,000 km and 60 days to 80 years in the Pacific Ocean. The relative roles of the ocean and atmosphere are interpreted using a stochastic upper-ocean temperature evolution model forced by noise terms representing intrinsic variability in each medium, defined using climate model data to produce realistic rather than white spectral power density distributions. The analysis of all datasets shows that the atmosphere dominates the SST and THF variability over zonal wavelengths larger than ~2,000–2,500 km. In HR and OBS, ocean processes dominate the variability of both quantities at scales smaller than the atmospheric first internal Rossby radius of deformation (R_1 , ~600–2,000 km) due to a substantial ocean forcing coinciding with a weaker atmospheric modulation of THF (and consequently of SST) than at larger scales. The ocean forcing also induces oscillations in SST and THF with periods ranging from intraseasonal to multidecadal, reflecting a red spectrum response to ocean forcing similar to that driven by atmospheric forcing. Such features are virtually absent in LR due to a weaker ocean forcing relative to HR.

Plain Language Summary This study investigates the importance of atmospheric processes (weather) and ocean currents in driving variations in sea surface temperature (SST) and the air-sea heat exchange at mid-latitudes. Our analysis uses satellite observations, a high-resolution (HR) climate model that resolves ocean currents with dimensions of tens of km, and a low-resolution model (LR) that can only simulate ocean currents with hundreds of km in size. We specifically examine the SST and heat exchange variability resolved by these datasets at horizontal scales between 50 and 10,000 km and time scales from 2 months to 80 years in the Pacific Ocean. Using a simple mathematical model to interpret the results, we find that variability at scales larger than 2,000 km is driven predominantly by weather. At smaller scales, SST and heat exchange are more variable in HR than in LR and agree better with satellite observations. We also find that ocean processes drive variability in SST with time scales ranging from 2 months to several decades, similar to those caused by weather, which in turn induces slow variations in the air-sea heat exchange.

1. Introduction

Interactions between the atmosphere and oceans largely determine the Earth's climate, and the physical mechanisms controlling these interactions are scale-dependent. In midlatitudes, at large spatial scales ($\mathcal{O}[10^3\text{km}]$), the atmosphere modulates the surface turbulent heat fluxes (THF) via the wind speed and the advection of humidity and air temperature by synoptic weather systems, producing slow fluctuations in sea surface temperature (SST) that lag the heat flux signal over time scales of several weeks or longer (e.g., Clement et al., 2015; Okumura

et al., 2001; Small et al., 2019; Xie, 2004). In turn, at ocean mesoscales ($\mathcal{O}[10^1 - 10^2 \text{ km}]$), ocean currents can create SST anomalies that are sufficiently intense and persistent to induce anomalous surface heat fluxes. The response in THF is forced by air-sea temperature and humidity differences that arise when an air parcel moves over mesoscale SST features, and is proportional to the magnitude of the underlying SST signal (e.g., Bishop et al., 2017; Putrasahan et al., 2017; Small et al., 2019; Villas Bôas et al., 2015). While the large-scale regime is traditionally considered important in climate dynamics, there is growing evidence that mesoscale air-sea coupling can influence oceanic and atmospheric variability (e.g., Chelton et al., 2004; Frenger et al., 2013; Gaube et al., 2015; Laurindo et al., 2019; Ma et al., 2016, 2017, 2015; O'Neill et al., 2010; Putrasahan et al., 2013, 2017) and play a key role in weather and climate (e.g., Chang et al., 2020; Kirtman et al., 2017; Ma et al., 2017, 2015; Minobe et al., 2008; Siqueira & Kirtman, 2016; Siqueira et al., 2021; Smirnov et al., 2015; Wills et al., 2016; Wills & Thompson, 2018; Yook et al., 2022).

Despite the importance of mesoscale air-sea interactions revealed by literature, the physical mechanisms that control the transition from large-scale to mesoscale air-sea coupling characteristics remain poorly understood. To investigate these mechanisms, this work uses spectral methods to characterize the SST and THF variability and co-variability resolved by satellite observations and climate model simulations over scales between 50 and 10,000 km and 60 days–80 years in the models and up to 13 years for observations. The roles of oceanic and atmospheric processes in shaping the variability revealed by each data set are then interpreted using an idealized stochastic climate model. The presented analysis focuses on the Pacific Ocean, although similar results and conclusions are also obtained for the Indian and Atlantic basins.

Several previous studies used stochastic climate models (Hasselmann, 1976) to analyze the local effects of the extratropical thermodynamic air-sea interactions (e.g., Barsugli & Battisti, 1998; Bishop et al., 2017; Dommenget & Latif, 2002; Frankignoul & Hasselmann, 1977; Frankignoul et al., 1998; Hall & Manabe, 1997; O'Reilly et al., 2016; Smirnov et al., 2014; Sun & Wu, 2021; Wu et al., 2006). These idealized models represent the mechanisms in the ocean and atmosphere that generate variability in the upper-ocean temperature as stochastic (i.e., random) processes, and indicate that THF drive SST anomalies when the atmosphere forcing signal is strong and vice-versa when the ocean forcing is strong. Stochastic models specifically predict, if THF is defined as positive when out of the ocean, that strong atmospheric forcing gives rise to negative correlations between the SST rate of change (known as the SST *tendency*) and THF at lag zero and to a lead-lag relationship between SST and THF. In turn, when the ocean forcing term is strong, positive correlations arise between SST and THF at lag zero while SST tendency and THF are related in a lagged fashion (cf. Figure 1 of Bishop et al., 2017).

Consistent with the conclusions drawn from idealized stochastic models, fully-coupled climate model simulations reproduce linear relationships characteristic of atmosphere- or ocean-driven variability depending on the resolution of their ocean components. When the resolution is insufficient to resolve mesoscale ocean eddies, linear SST/THF relationships suggest that the variability is primarily driven by the atmosphere over much of the extratropics. In contrast, horizontal ocean resolutions sufficiently refined to allow eddy formation and evolution significantly enhance the mesoscale current variability (Constantinou & Hogg, 2021; Sérazin et al., 2015, 2018), which increases the local upper-ocean heat convergence anomalies that in turn lead to larger SST variability, most prominently in strong current systems such as the seaward extensions of western boundary currents and the Antarctic Circumpolar Current (ACC) (Constantinou & Hogg, 2021; Putrasahan et al., 2017; Sérazin et al., 2017; Small et al., 2020; Smirnov et al., 2014). The SST variability at these regions is positively correlated with THF (Chang et al., 2020; Kirtman et al., 2012; Ma et al., 2016; Roberts et al., 2016), a characteristic that is also present in satellite estimates (Bishop et al., 2017; Ma et al., 2016; Small et al., 2019; Villas Bôas et al., 2015), suggesting that the mesoscale air-sea coupling regime is dominant there.

Recently, several studies examined the spatial and temporal scales where ocean dynamics can influence the extratropical SST variability and consequently impact THF. For instance, the analysis of satellite data indicate that ocean processes dominate the variability of both quantities over spatial scales smaller than $\sim 500\text{--}700$ km at most latitudes, with their importance increasing toward interannual timescales (Bishop et al., 2017; Small et al., 2019). In support of these observational findings, eddy-resolving ocean-only simulations indicate that mesoscale currents enhance the variability in upper-ocean heat content and SST over spatial scales smaller than about 1,000 km and timescales up to decadal in regions with strong extratropical current systems (Constantinou & Hogg, 2021; Sérazin et al., 2017, 2018). Fully-coupled simulations show similar results, and further indicate that the THF variability is also enhanced (Chang et al., 2020; Small et al., 2020). The importance of ocean

phenomena on driving changes in SST and THF over intraseasonal to interannual timescales was also revealed in an eddy-resolving coupled simulation of an idealized western boundary current system (Martin et al., 2021) and by the Estimating the Circulation and Climate of the Ocean (ECCO) ocean state estimate in the Gulf Stream and subpolar North Atlantic (Buckley et al., 2014, 2015) and in the extratropics including oceanic regions away from strong currents (Patrizio & Thompson, 2021, 2022).

The results from these previous studies indicate that ocean processes can overcome the large-scale, atmosphere-driven modulation of THF and SST over spatial and temporal scales that are larger and longer (potentially much more so) than that of individual mesoscale eddies. They also indicate that, although the main differences between the large-scale and mesoscale air-sea coupling regimes are well established, the spatial and temporal scales where each regime prevails are still not well characterized, nor are the physical mechanisms that give rise to their scale dependence. This work addresses these gaps. The main hypotheses are:

1. The relative importance of ocean processes driving the SST and THF variability increases toward the ocean mesoscales due to a strong intrinsic ocean variability coinciding with a weaker atmospheric modulation of THF (and consequently of SST) than at larger spatial scales;
2. Ocean processes induce low-frequency SST fluctuations via a mechanism similar to that caused by atmospheric stochastic forcing (Frankignoul & Hasselmann, 1977; Hasselmann, 1976), where the large heat capacity of the upper-ocean integrates the forcing noise to produce a red spectrum response in SST. THF mirrors this red spectrum response owing to its dependence on SST.

The present study tests these hypotheses by examining the SST and THF power spectra and cross-spectral statistics resolved by a satellite product and by fully-coupled climate model simulations run with eddy-resolving and eddy-parameterized horizontal ocean resolutions. The obtained spectral quantities are interpreted using a stochastic model of air-sea interactions forced by noise terms representing the action of atmospheric and oceanic processes. Here, the noise terms are defined with realistic variance distributions as a function of frequency and zonal wavenumber taken from the climate model simulations. This approach contrasts with that typically adopted in the literature, where the forcing terms are represented as randomly-generated white noise signals with variances approximately constant across all scales (e.g., Bishop et al., 2017; Frankignoul et al., 1998; Sun & Wu, 2021; von Storch, 2000; Wu et al., 2006).

The remainder of this paper is organized as follows: Section 2 describes the satellite and climate model data sets used (2.1), the spectral data analysis methods (2.2), and the methods involved in the stochastic climate model analysis (2.3). Section 3 first briefly describes the global SST and THF variance distribution resolved by the satellite and model datasets (3.1). It then presents the power spectral densities and cross-spectral statistics computed using SST and THF data, as well as corresponding estimates predicted using the stochastic model (3.2). Section 4 discusses the results in light of the existing literature, and Section 5 summarizes this study and its conclusions.

2. Methods

2.1. Data Description

2.1.1. J-OFURO3 Observational Product

Observational estimates of SST and THF are from the Japanese Ocean Flux Data Sets with Use of Remote-Sensing Observations version 3 (J-OFURO3, Tomita et al., 2019). Briefly, the J-OFURO3 dataset gives estimates of THF (defined as positive upwards) and its components. THF is estimated using the COARE 3.0 bulk formulations (Fairall et al., 2003), whose variables are retrieved from various satellite data sources except for 2-m air temperature, which is from the National Centers for Environmental Prediction-Department of Energy Atmospheric Model Intercomparison Project reanalysis model (NCEP-DOE AMIP-II, Kanamitsu et al., 2002). In turn, SST is the daily median of values taken from multiple satellite missions and regularly-gridded SST products, an approach designed to provide a robust SST estimate while minimizing uncertainties intrinsic to any single data source (Kubota et al., 2002; Tomita et al., 2019). The J-OFURO3 data (OBS) used in this study was produced at a $0.25^\circ \times 0.25^\circ \times 1$ -month resolution for January 1988 to December 2013.

2.1.2. CESM1.3 Climate Model Simulations

This study uses climate simulations generated with the Community Earth System Model version 1.3 (CESM1.3, Meehl et al., 2019; Zhang et al., 2020) by the International Laboratory for High-Resolution Earth System Prediction (iHESP, Chang et al., 2020). The CESM1.3 is a global climate model composed of the Community Atmosphere Model version 5 (Neale et al., 2012), the Parallel Ocean Program version 2 (Danabasoglu et al., 2012; Smith et al., 2010), the Community Ice Code version 4 (Hunke & Lipscomb, 2010), and the Community Land Model version 4 (Lawrence et al., 2011). The model components exchange state information and fluxes via the CESM Coupler 7, which computes the fluxes at the air-sea interface using the Large and Yeager (2004) bulk parameterizations.

Outputs from two iHESP CESM1.3 preindustrial control simulations are analyzed, run at contrasting horizontal resolutions in the ocean and atmosphere. The first (low-resolution, LR) uses a nominal 1° horizontal resolution in both model components that cannot resolve mesoscale ocean eddies, whose effects are parameterized (Gent & McWilliams, 1990). The second (high-resolution, HR) is configured with a nominal 0.25° horizontal resolution in the atmosphere and 0.1° in the ocean, which is eddy-resolving in the ocean except at high latitudes. Both the HR and LR experiments use an atmospheric CO_2 concentration fixed at 1850 levels and are integrated for 500 years (Chang et al., 2020).

The HR and LR data used in this work are monthly global fields of SST, THF, and 2-m height humidity, and three-dimensional monthly global fields of ocean heat flux convergence (OHFC), computed using horizontal and vertical components of the heat flux, that are vertically-integrated for the upper 50-m of the water column. The 50-m integration level is chosen for consistency with the stochastic climate model formulation described in Section 2.3. All quantities obtained from LR (HR) are mapped onto a regular $1^\circ \times 1^\circ$ ($0.25^\circ \times 0.25^\circ$) spatial grid and are retrieved for the simulation years 21–500 (338–500) based on their availability in the model output files.

2.2. Spectral Analysis

This work examines the power spectra of SST and THF and their cross-spectra in HR, LR, and OBS as a function of frequency and zonal wavenumber. This spectral analysis is similar to that described in Laurindo et al. (2019) for SST and 10-m wind speed. More specifically, it examines spectra varying as a function of both zonal wavenumber and frequency (k and ω , respectively) computed from zonal-temporal (x, t) data series of the considered quantities obtained at every 1° (0.25°) latitude in LR (HR and OBS) between 55°S and 60°N in the Pacific Ocean. This analysis is performed within a Pacific basin mask (shown below in Figure 2h) that excludes regions shallower than 1,000-m around the continental shelves to avoid the influence of coastal processes. The mask also ignores small islands at the basin's interior, whose gaps in the data are filled using linear interpolation.

The zonal-temporal data series of SST and THF obtained at each latitude increment have their means removed along both (x, t) directions. A best-fit model composed of a linear temporal trend and of annual and semiannual harmonics (to represent seasonal variations) is also removed. It is noted that, differently from HR and LR, OBS include anthropogenic climate change signals that are not properly removed using a simple linear trend. More advanced methods for retrieving anthropogenic signals from the data are presented and discussed in Frankignoul et al. (2017) and Deser and Phillips (2021), but are not used here.

The resulting SST and THF anomaly data series [$T(x, t)$ and $Q(x, t)$, respectively] are then subdivided into 80-year segments for HR and LR, and into 13-year segments for OBS, with a 50% temporal overlap. The resulting data segments are selected within 4° meridional bands centered at each grid point of the latitudinal axis, forming ensembles containing multiple realizations of $T(x, t)$ and $Q(x, t)$ (48 for HR, 44 for LR, and 48 for OBS), that are used to compute the spectral functions at each latitude—that is, results obtained at 10°N are computed using data from latitudes between 8°N and 12°N .

Following Bendat and Piersol (1986), the power spectral density functions (also known as autospectral density functions) of $T(x, t)$ and $Q(x, t)$ are defined as:

$$G_{TT}(k, \omega) = \frac{2}{l_k l_\omega} \langle |\tilde{T}(k, \omega)|^2 \rangle, \text{ and} \quad (1)$$

$$G_{QQ}(k, \omega) = \frac{2}{l_k l_\omega} \langle |\tilde{Q}(k, \omega)|^2 \rangle, \quad (2)$$

where the tilde denotes a two-dimensional Fourier transform to the k and ω domains, l_k is the length of \tilde{T} and \tilde{Q} in the zonal wavenumber domain, and l_ω is their length in frequency domain. The brackets represent ensemble-averages over the $|\tilde{T}(k, \omega)|^2$ and $|\tilde{Q}(k, \omega)|^2$ realizations.

Similarly, the cross-spectral density function between $T(x, t)$ and $Q(x, t)$ is:

$$G_{TQ}(k, \omega) = \frac{2}{l_k l_\omega} \langle \tilde{T}^*(k, \omega) \tilde{Q}(k, \omega) \rangle, \quad (3)$$

where the asterisk denotes complex conjugation.

The spectral functions are computed as functions of both k and ω , which are integrated in frequency domain to obtain estimates as a function of zonal wavenumber and latitude. The spectral functions are also separately integrated in the zonal wavenumber domain to obtain estimates as a function of frequency and latitude.

The integrated estimates are then used to compute the magnitude-squared coherence γ_{TQ}^2 as:

$$\gamma_{TQ}^2 = \frac{|G_{TQ}|^2}{G_{TT}G_{QQ}}, \quad (4)$$

where $G_{TQ} = |G_{TQ}|e^{-i\theta_{TQ}}$, with θ_{TQ} (known as phase factor) describing the phase relationship between the sinusoidal components of \tilde{T} and \tilde{Q} . γ_{TQ}^2 varies between zero and one, reflecting the fraction of the variance of Q that can be explained by T for each spectral coordinate.

2.3. Stochastic Upper-Ocean Temperature Anomaly Model

2.3.1. Model Description

This work uses a stochastic model for the upper-ocean temperature evolution proposed by Frankignoul et al. (1998) (hereafter FCL98) to guide the physical interpretation of the spectral quantities computed using SST and THF data from OBS, HR, and LR (Section 2.2). Here, quantities predicted using the FCL98 model are distinguished from those obtained using SST and THF data by variables adorned by primes.

The FCL98 formulation can be written as:

$$\rho_0 c_p h \frac{\partial T'}{\partial t} = N_a + N_m - (\lambda_q + \lambda_0) T', \quad (5)$$

where T' is the temperature of a well-mixed upper-ocean layer of thickness h , density ρ_0 , and specific heat c_p . N_a represents the stochastic forcing of the THF by intrinsic atmospheric variability, and N_m denotes the forcing by other processes, identified in FCL98 as primarily representing the action of wind stress variability. Lastly, λ_q and λ_0 are feedback factors responsible for damping the temperature anomalies, the former associated with THF and the latter to terms unrelated to the air-sea fluxes, such as radiative cooling and turbulent mixing.

In this work, Equation 5 is modified by attributing the origin of the N_m stochastic forcing term to internal ocean variability (thus renaming it N_o), the origin of the λ_0 feedback factor solely to radiative cooling (being renamed λ_r), and by considering that the stochastic forcing term N_a represents stochastic variability in the near-surface atmospheric temperature rather than in THF, approach similar to that used in Barsugli and Battisti (1998). With these, Equation 5 becomes:

$$\frac{\partial T'}{\partial t} = -\alpha (T' - N_a) - \beta T' + \nu N_o, \quad (6)$$

Table 1
Values of the FCL98 Model Parameters (Equations 6–9)

Parameter	Value
ρ_0	1,025.0 kg m ⁻³
c_p	3,900.0 J kg ⁻¹ K ⁻¹
H	50.0 m
Λ	23.4 W m ⁻² K ⁻¹
λ_r	1.3 W m ⁻² K ⁻¹

where $\nu = 1/(\rho_0 c_p h)$, $\alpha = \lambda_q \nu$, and $\beta = \lambda_r \nu$. Here, THF is defined as $Q' = \lambda_q (T' - N_a)$, with positive values denoting fluxes out of the ocean. The values of the coefficients α , β , ν , and λ_q are computed for a $h = 50$ -m thick ocean layer as described in Barsugli and Battisti (1998), and are listed in Table 1.

The stochastic model defined in Equation 6 was developed for mid-latitudes and is unable to represent important air-sea coupling mechanisms at work within the tropics, such as the Bjerknes feedback and the Wind-Evaporation-Sea Surface Temperature (WES) feedback (e.g., Mahajan et al., 2009). For this reason, the present work uses Equation 6 to support the interpretation of spectral estimates obtained at latitudes poleward of 15°. Other limitations are discussed in Section 4.3.

Next, Equation 6 is Fourier transformed to zonal wavenumber and frequency domains (k , ω) and used to obtain analytical expressions for the power spectrum of the upper-ocean mixed-layer temperature T' (G'_{TT}), the power spectrum of the surface turbulent heat flux Q' (G'_{QQ}), and the cross-spectrum between T' and Q' (G'_{TQ}), given by:

$$G'_{TT} = \frac{2}{l_k l_\omega} \left[\frac{v^2 \langle |\tilde{N}_o|^2 \rangle + \alpha^2 \langle |\tilde{N}_a|^2 \rangle}{4\pi^2 \omega^2 + (\alpha + \beta)^2} \right], \quad (7)$$

$$G'_{QQ} = \frac{2\lambda_q^2}{l_k l_\omega} \left[\frac{v^2 \langle |\tilde{N}_o|^2 \rangle + (4\pi^2 \omega^2 + \beta^2) \langle |\tilde{N}_a|^2 \rangle}{4\pi^2 \omega^2 + (\alpha + \beta)^2} \right], \text{ and} \quad (8)$$

$$G'_{TQ} = \frac{2\lambda_q}{l_k l_\omega} \left[\frac{v^2 \langle |\tilde{N}_o|^2 \rangle + \alpha(i2\pi\omega - \beta) \langle |\tilde{N}_a|^2 \rangle}{4\pi^2 \omega^2 + (\alpha + \beta)^2} \right], \quad (9)$$

where \tilde{N}_o and \tilde{N}_a are Fourier transformed stochastic noise terms, and $\langle |\tilde{N}_o|^2 \rangle$ and $\langle |\tilde{N}_a|^2 \rangle$ are their power spectra.

Cross-terms between \tilde{N}_o and \tilde{N}_a are small by design assuming that intrinsic variability in the ocean and the atmosphere are unrelated to each other, and are thus omitted in Equations 7–9. The analytical expressions shown in Equations 7–9 are also substituted in Equation 4 to obtain stochastic model estimates of coherence (γ'_{TQ}) and phase factor (θ'_{TQ}).

2.3.2. White Noise Versus “Geophysical” Noise Forcing Spectra

In the context of air-sea interactions, previous studies have defined stochastic models varying solely as a function of time, representing the forcing by oceanic and atmospheric processes as stochastic signals with a “white” spectral power density in frequency space—that is, with approximately the same variance (power) at every frequency. While observations support the white noise assumption in frequency space (e.g., Frankignoul et al., 1998; Patrizio & Thompson, 2022), they also show that the spectra of intrinsic atmospheric and oceanic motions are “red” in wavenumber space, with more variance at larger wavelengths (e.g., Ducet et al., 2000; Nastrom & Gage, 1985). The variance distribution in wavenumber space also differ between each medium, likely reflecting the distinct intrinsic scales of synoptic weather systems and mesoscale ocean eddies. This work hypothesizes that these distinct variance distributions in time and space can give rise to the spatial scale dependence of thermodynamic air-sea interactions revealed by recent assessments (Bishop et al., 2017; Laurindo et al., 2019; Small et al., 2019, 2020).

To test this hypothesis, data from HR and LR are used to attribute realistic variance distributions in zonal wavenumber and frequency domains to the $\langle |\tilde{N}_o|^2 \rangle$ and $\langle |\tilde{N}_a|^2 \rangle$ forcing spectra in Equations 7–9, hereafter referred to as “geophysical noise” spectra. More specifically, 2-m height specific humidity is used to define the geophysical noise $\langle |\tilde{N}_a|^2 \rangle$ considering that (a) this quantity is related to the latent turbulent heat flux bulk formulation (Fairall et al., 2003; Large & Yeager, 2004) in the same way as N_a is related to Q' in Equation 6; (b) the latent heat fluxes are usually larger than the sensible heat fluxes; and (c) time-domain correlations and coherence estimates show

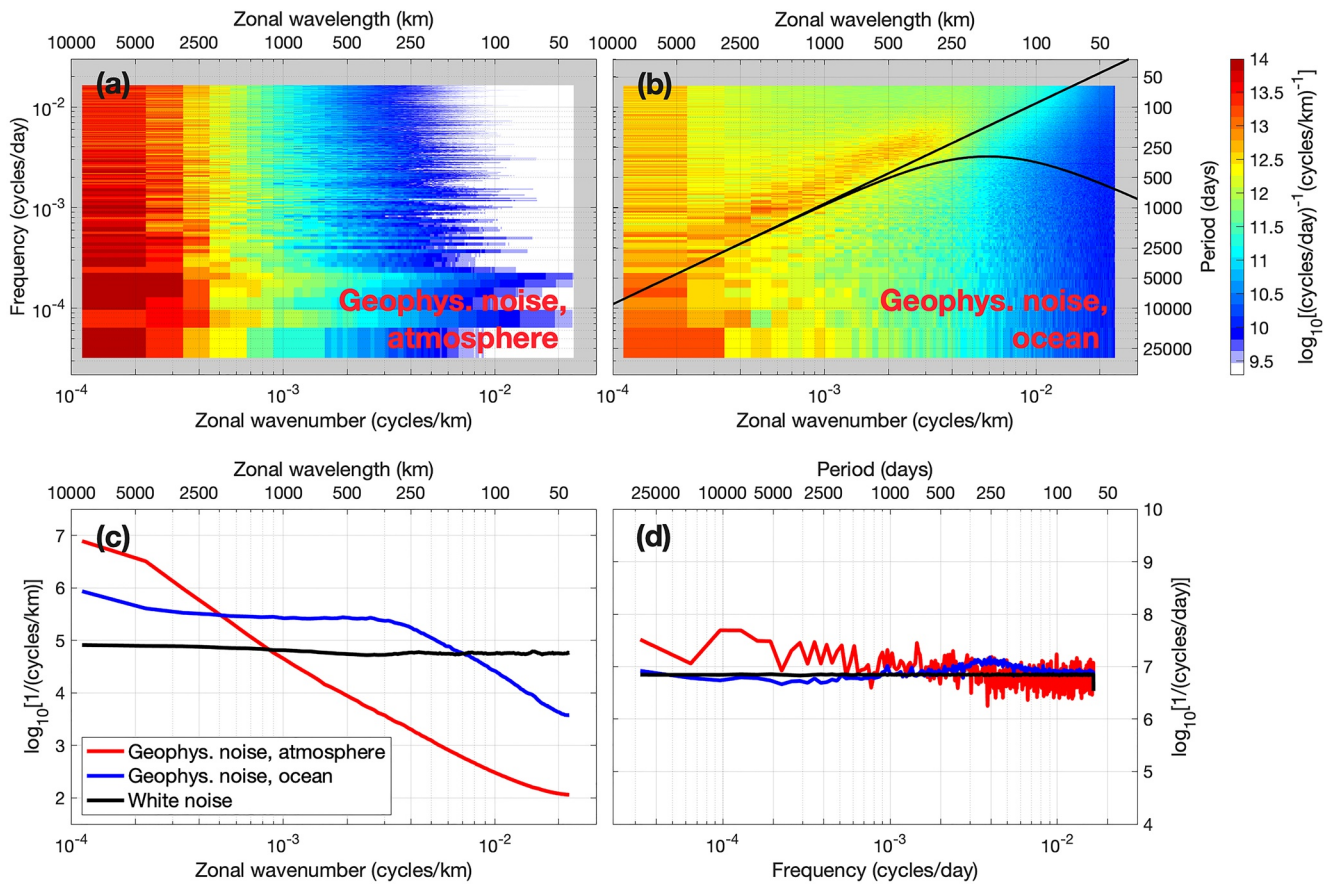


Figure 1. Geophysical noise power spectra for high-resolution (HR) and 40°S in the Pacific Ocean. The top panels show estimates obtained as a function of both zonal wavenumber (k) and frequency (ω) for the atmosphere and ocean (panels a and b, respectively). The curved line in (b) represent the dispersion relation for first mode baroclinic oceanic Rossby waves while the straight line is the non-dispersive wave limit. The bottom panels show estimates integrated over one dimension to highlight their variation as a function of either k or ω (panels c and d, respectively). Here, the red and blue lines represent geophysical noise spectra for the atmosphere and the ocean, respectively, and the black lines are corresponding white noise estimates. To emphasize their distinct spectral structures, all depicted estimates are computed using normalized data with variances equal to one.

that the 2-m height specific humidity variability is weakly related to (and thus largely independent from) mesoscale SST anomalies in most oceanic regions (not shown), suggesting that atmospheric processes predominantly drives its variability. In turn, OHFC is used to define the geophysical noise ($|\tilde{N}_o|^2$) considering that this quantity corresponds to the main driver of mesoscale SST variability (Putrasahan et al., 2017; Small et al., 2020).

The specific methods used to define the geophysical noise spectra are described in Appendix A. The obtained estimates and their differences relative to white noise spectra are illustrated in Figure 1 for HR and 40°S in the Pacific, a latitude chosen to demonstrate characteristics that are representative of the extratropics.

First considering the atmospheric forcing spectra ($\langle |\tilde{N}_a|^2 \rangle$), the geophysical noise estimate includes slightly larger variances toward lower frequencies than a white noise spectrum—thus, it is slightly red (Figure 1d). The enhanced low-frequency variance can potentially arise from the coupled nature of the CESM simulations, considering that the stochastic model analysis by Barsugli and Battisti (1998) predicted that the air-sea thermal coupling would lead to a red rather than white spectral response in the near-surface air temperature, a property closely associated with near-surface humidity. In contrast, the geophysical noise ($|\tilde{N}_o|^2$) is prominently red in zonal wavenumber domain, with the power decaying toward higher wavenumbers at an approximate k^{-3} rate over scales $\sim 1,000$ –4,000 km and at a slower k^{-2} rate over scales smaller than 1,000 km (Figure 1c). This distribution resembles that retrieved for tropospheric winds using aircraft measurements (Callies et al., 2014; Cho et al., 1999; Nastrom & Gage, 1985; Tulloch & Smith, 2009), although the latter was found to decay at a $k^{-5/3}$ rate over scales smaller than 1,000 km. The geophysical noise ($\langle |\tilde{N}_a|^2 \rangle$) estimate for LR is similar and is omitted for brevity.

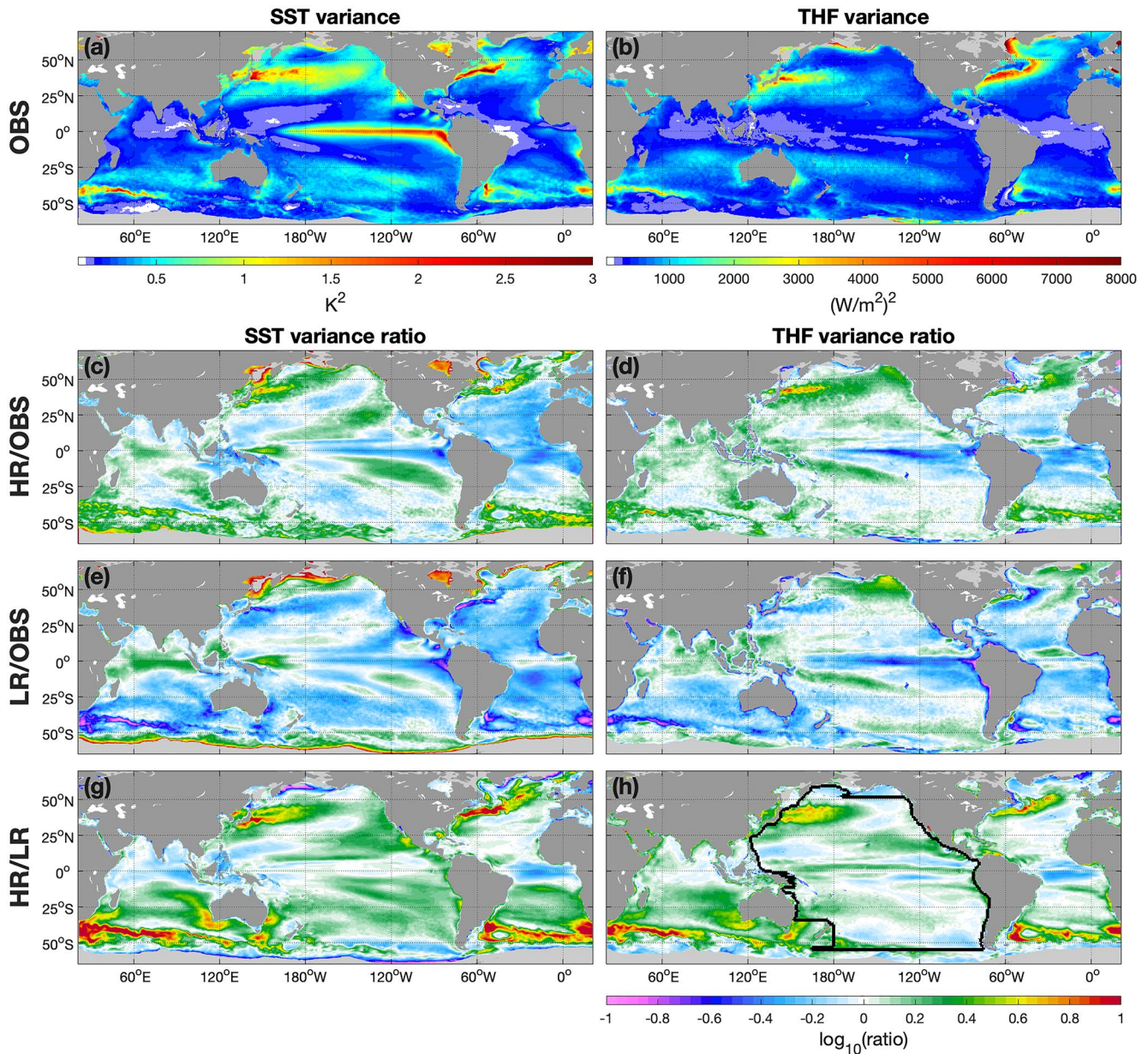


Figure 2. Global maps of the monthly sea surface temperature (SST) and turbulent heat flux (THF) variances resolved by the J-OFURO3 satellite product (satellite observations (OBS), panels (a) and (b), respectively), and the ratios of the corresponding variances resolved by the high-resolution (HR) (c–d) and low-resolution (LR) (e–f) to those of respective OBS. Panels (g) and (h) show the ratios between the variances resolved in HR and LR. The black contour in (h) delineates the basin mask for the Pacific Ocean used for the zonal-temporal spectral analysis.

In turn, the geophysical noise ocean forcing spectra $\langle |\tilde{N}_o|^2 \rangle$ is nearly white in frequency space (Figure 1d). In zonal wavenumber domain, it has a plateau between ~ 300 and $6,000$ km and a k^{-2} slope at smaller spatial scales (Figure 1c). The spectrum computed as a function of both k and ω (Figure 1b) show that the variances are larger near the non-dispersive portion of the dispersion relation for first mode baroclinic Rossby waves, here computed using an observational climatology of the first internal Rossby radius of deformation (Chelton et al., 1998). This correspondence was also reported in satellite-based estimates of SST, sea surface height, ocean color (Chelton, Gaube, et al., 2011; Chelton, Schlax, & Samelson, 2011; Early et al., 2011; O’Brien et al., 2013), and in positively-correlated SST and 10-m wind signals (Laurindo et al., 2019). Forms of ocean variability with these dispersion characteristics include not only linear Rossby waves, but also nonlinear mesoscale ocean phenomena such as coherent eddies and zonal jets (Berloff & Kamenkovich, 2013b, 2013a; Chelton, Gaube,

et al., 2011; Early et al., 2011; Laurindo et al., 2019; Polito & Sato, 2015). Here, the larger variances near the Rossby wave dispersion relation is observed over much of the extratropics except at the latitudes of strong current systems such as the ACC and the Kuroshio Current, potentially owing to the influence of strong zonal flows in the dispersion characteristics (Laurindo et al., 2019). The corresponding $\langle |\tilde{N}_o|^2 \rangle$ estimate for LR (not shown) reveal characteristics similar to those described for HR, except that it decays at an $\sim k^{-1}$ rate over zonal wavelengths between ~ 600 and $6,000$ km.

The differences between stochastic model estimates computed using geophysical and white noise forcing are analyzed in the Supporting Information S1. In frequency domain, both types of forcing noise produce similar results because the geophysical noise is approximately white. In contrast, variations of G'_{TT} , G'_{QQ} , γ'_{TQ} , and θ'_{TQ} as a function of zonal wavenumber are only present in estimates obtained using geophysical noise (Figures S1–S4 in Supporting Information S1). That is because the FCL98 stochastic model solutions do not depend on zonal wavenumber by construction (Equations 7–9), and variations as a function of k have their sole origins in the forcing noise. The next Section shows that stochastic model estimates forced by geophysical noise reproduce key characteristics of the SST and THF spectra resolved by satellite and climate model data, and can thus be used to support their physical interpretation.

3. Results

3.1. SST and THF Variances From Observations, HR, and LR

To provide a background to the analysis of the spectral quantities computed using HR, LR, and OBS data, this Section briefly describes the horizontal distributions of the monthly SST and THF variances for each of the datasets.

The SST variance from OBS is larger in strong current systems and in the tropics (Figure 2a). More specifically, the largest values (>1.0 K²) coincide with western boundary currents and their seaward extensions, the equatorial current system in the Pacific, the ACC, the Brazil-Malvinas Confluence, and the Agulhas Retroflexion. Within the Tropical Pacific, high variances are associated with El Niño-Southern Oscillation (ENSO) events and with zonally-propagating intraseasonal Rossby waves and Tropical Instability Waves (TIWs), while at the extratropical current systems it is predominantly driven by mesoscale ocean phenomena such as coherent eddies and meanders. Away from these energetic systems, variances of $O(0.1-1.0$ K²) are found within the subtropical gyres of all major ocean basins. Over monthly timescales, the SST variability in these regions is predominantly driven by the atmosphere via THFs (Bishop et al., 2017; Small et al., 2019), although it also includes the signature of westward-propagating ocean eddies (Chelton, Schlax, & Samelson, 2011; Laurindo et al., 2019). The THF variance from OBS (Figure 2b) noticeably lacks the enhanced variances at the tropical Pacific found in the SST estimates, but similar spatial features (as in SSTs) are found in the extratropics. THF variances of $\sim 1,000-5,000$ (W/m²)² are seen in the Labrador Sea and at strong current systems, most prominently the Gulf Stream and the Kuroshio Currents, while the interior of the subtropical gyres show values between ~ 500 and $1,500$ (W/m²)².

The SST and THF variance distributions in HR are similar to that of OBS, although the HR values can be two to 10 times larger than OBS within the extratropical current systems (Figures 2c and 2d). In contrast, the lack of resolved mesoscale phenomena in LR leads to the underestimation of the SST and THF variances relative to HR and OBS over much of the extratropics, specifically by factors of ~ 10 in the eddy-rich regions and of ~ 2 within the subtropical gyres (Figures 2e–2h). Previous assessments showed that the higher SST variability in HR relative to LR is caused by the larger upper-ocean heat flux convergence by the resolved mesoscale ocean variability, which in turn increases the THF variability (Kirtman et al., 2012; Putrasahan et al., 2017; Small et al., 2019, 2020). The results of the spectral analysis, described next, determines the spatial and temporal scales where resolved ocean phenomena induce such a response in both quantities.

3.2. Power Spectra and Cross-Spectral Statistics

3.2.1. Zonal Wavenumber Spectra

The zonal wavenumber SST power spectra (G_{TT}) from all datasets (HR, LR, and OBS) show similar magnitudes at zonal wavelengths between $\sim 2,500$ and $7,000$ km and vary at a k^{-3} rate, as seen at 40°S (Figure 3a).

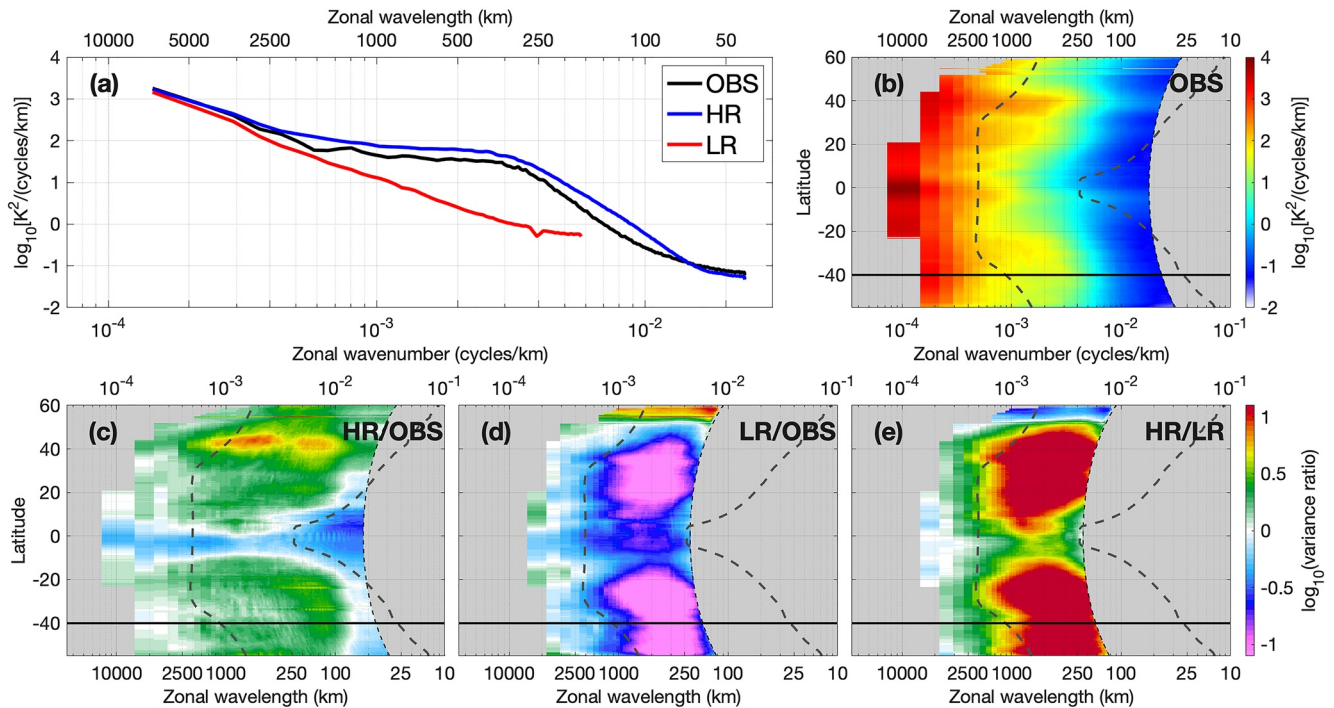


Figure 3. Sea surface temperature (SST) power spectra (G_{TT}) computed as a function of zonal wavenumber for the Pacific Ocean using high-resolution (HR), low-resolution (LR), and satellite observations (OBS) data. Panel (a) show estimates for 40°S, (b) is the latitudinal spectrogram for OBS (c–d) show the ratio of the OBS estimates relative to the HR and LR results, and (e) the ratio between the HR and LR results. The left and right thick dashed lines in (b–e) represent the zonally-averaged first internal Rossby radius of deformation for the atmosphere and the ocean, respectively, the thin dashed line marks the spatial Nyquist frequency for the spectral analysis, and the black horizontal line marks the 40°S latitude.

Toward smaller scales, HR and OBS estimates noticeably diverge from LR, showing a plateau between ~ 300 and 2000 km and then decaying at a $\sim k^{-4}$ rate between ~ 70 and 300 km while in LR they maintain the k^{-3} slope until ~ 300 km. These distinct shapes result in a much larger SST variance in HR and OBS relative to LR over scales smaller than about $2,000$ km. Similar results are found for the THF power spectra (G_{QQ}) (not shown).

The spectrograms of G_{TT} as a function of latitude (Figures 3b–3e) indicate that the spectral characteristics observed at 40°S occur over much of the extratropics. The same is observed in corresponding G_{QQ} estimates (not shown). To support the interpretation of the spectrograms, they are overlaid by the meridional profile of the zonally-averaged first internal Rossby radius of deformation (R_1) for the atmosphere and the ocean. Here, the atmospheric R_1 is computed using time-averaged potential temperature data for the troposphere obtained from the National Centers for Environmental Prediction (NCEP) reanalysis model (Kalnay et al., 1996), while the oceanic R_1 is taken from the Chelton et al. (1998) observational climatology.

The ratio between the power spectra resolved by each data set indicate that the largest differences between HR and OBS relative to LR (factors of 10 or more) usually occur at wavelengths smaller than the atmospheric R_1 , which increases from ~ 600 km at 60° latitude in both hemispheres to $\sim 2,000$ km within the tropics. Despite the SST and THF spectra resolved by HR being closer in magnitude and overall shape to OBS than LR, in the extratropics they exceed the magnitude of OBS at most wavenumbers. This characteristic is most prominent at the latitudes of strong current systems, such as between 35 and 50°N where the seaward extensions of the Kuroshio and Oyashio Currents occur (Figure 3c). The ratio between the SST (THF) variances resolved by HR and OBS, averaged over all latitudes and wavenumbers, is 1.60 (1.13). For 35 – 50°N , the ratio increase to 2.69 (2.16).

For all of the datasets, the coherence (γ_{TQ}^2) at zonal wavelengths larger than approximately $2,000$ km is low (~ 0.2 and the phase ($|\theta_{TQ}|$) is $\sim 90^\circ$ (Figure 4). A detailed examination at 40°S (Figures 4a and 4b) shows that, toward smaller scales, γ_{TQ}^2 increases in HR and OBS reaching ~ 0.9 between 250 and 500 km, while $|\theta_{TQ}|$ approaches zero. At scales smaller than 250 km, the coherence in OBS steadily decrease until ~ 0.2 at about 100 km. The coherence is larger in HR than in OBS over most wavelengths, maintaining values above 0.7 at 100 km, which then sharply

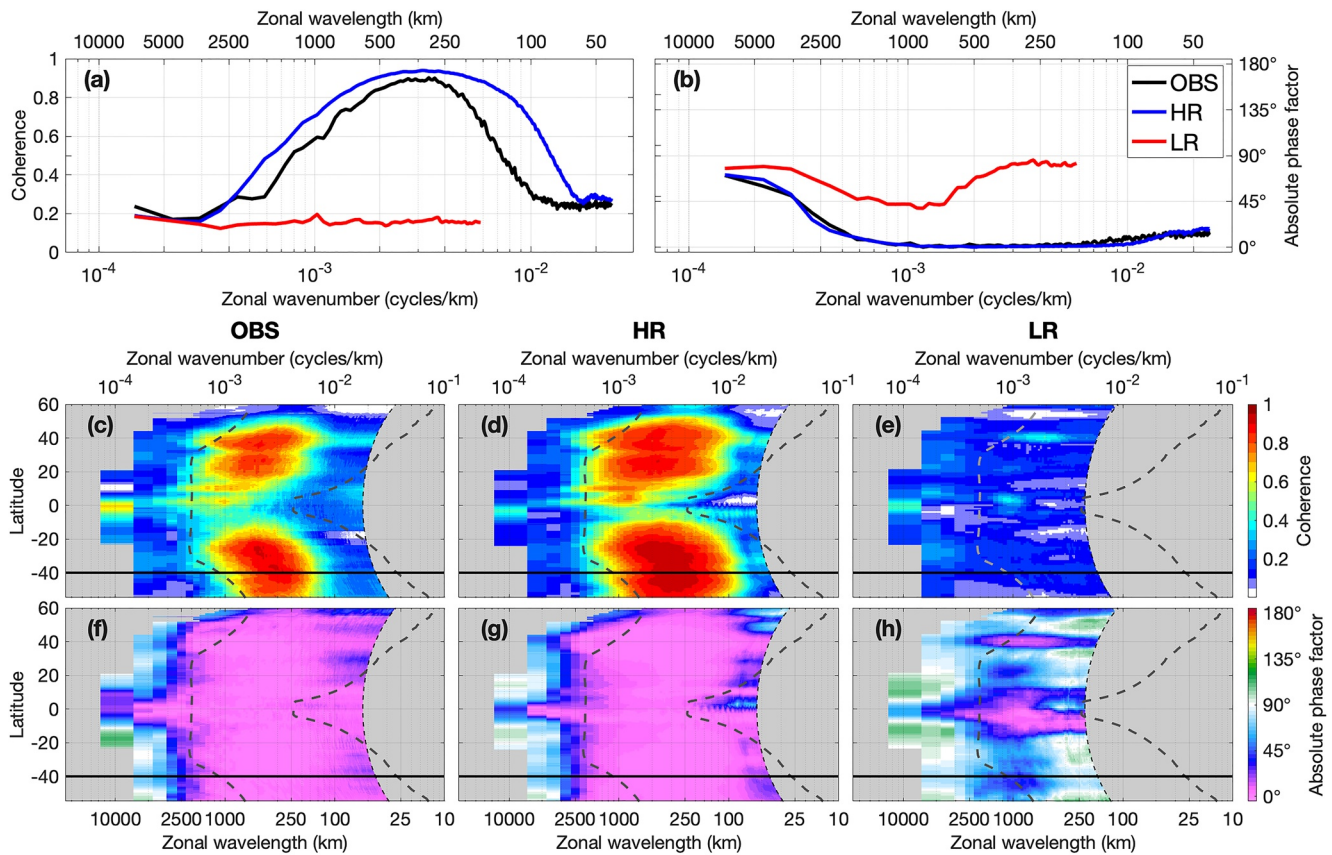


Figure 4. Coherence (γ_{TQ}^2) and absolute phase factor (θ_{TQ}) between sea surface temperature (SST) and turbulent heat flux (THF) in zonal wavenumber domain for the Pacific Ocean resolved by high-resolution (HR), low-resolution (LR), and satellite observations (OBS). The top row (a–b) exemplify estimates for 40°S while the middle (c–e) and bottom (f–h) rows show latitudinal spectrograms. The left and right thick dashed lines in (c–h) represent the zonally-averaged first internal Rossby radius of deformation for the atmosphere and the ocean, respectively; the thin black dashed denotes the spatial Nyquist frequency for the spectral analysis; and the black horizontal line marks the 40°S latitude that the estimates in panels (a–b) refer to.

decreases to ~ 0.2 near the limit of the analysis at approximately 50 km. In contrast, LR at 40°S shows a coherence of about 0.2 throughout the analyzed wavenumber range, with minimum phase factors of about 50° between ~ 700 and 2,500 km that return to 90° toward smaller scales.

The latitudinal spectrograms of γ_{TQ}^2 and $|\theta_{TQ}|$ (Figures 4c–4h) indicate that OBS and HR resolves the band of high coherences associated with near-zero phase factors at most latitudes, with the largest γ_{TQ}^2 values (>0.5) observed in the extratropics and over spatial scales smaller than the atmospheric R_1 . Interestingly, the LR results also show smaller phase factors at smaller spatial scales in the extratropics, with $|\theta_{TQ}|$ approaching zero at the latitudes of the Kuroshio and Oyashio Currents ($\sim 35^\circ\text{--}50^\circ\text{N}$) and within the tropics, both features associated with coherences of about 0.4.

To enable a physical interpretation of the spectra computed using OBS, HR, and LR data, Figures 5 and 6 show corresponding estimates obtained using the FCL98 stochastic model. Recall that stochastic model estimates are represented by variables adorned by primes (hence G'_{TT} , G'_{QQ} , γ'^2_{TQ} , and $|\theta'_{TQ}|$). Further, OCN denotes stochastic model estimates computed using solely the oceanic noise forcing spectra $\langle |\tilde{N}_o|^2 \rangle$, where the atmospheric forcing spectra $\langle |\tilde{N}_a|^2 \rangle = 0$, and ATM denotes estimates obtained using solely $\langle |\tilde{N}_a|^2 \rangle$, where $\langle |\tilde{N}_o|^2 \rangle = 0$.

The G'_{TT} estimate for HR at 40°S (Figure 5a) indicates that ATM has larger magnitudes than OCN at zonal wavelengths longer than $\sim 2,500$ km. Toward smaller scales, the variance in ATM decreases steeply at an approximate k^{-3} rate and is then surpassed by OCN, which accounts for the plateau observed between ~ 300 and 2,000 km—hence implying that this feature arises from the action of ocean processes. Corresponding results for LR (Figure 5b) has an ATM component similar in shape and magnitude to that obtained for HR, however

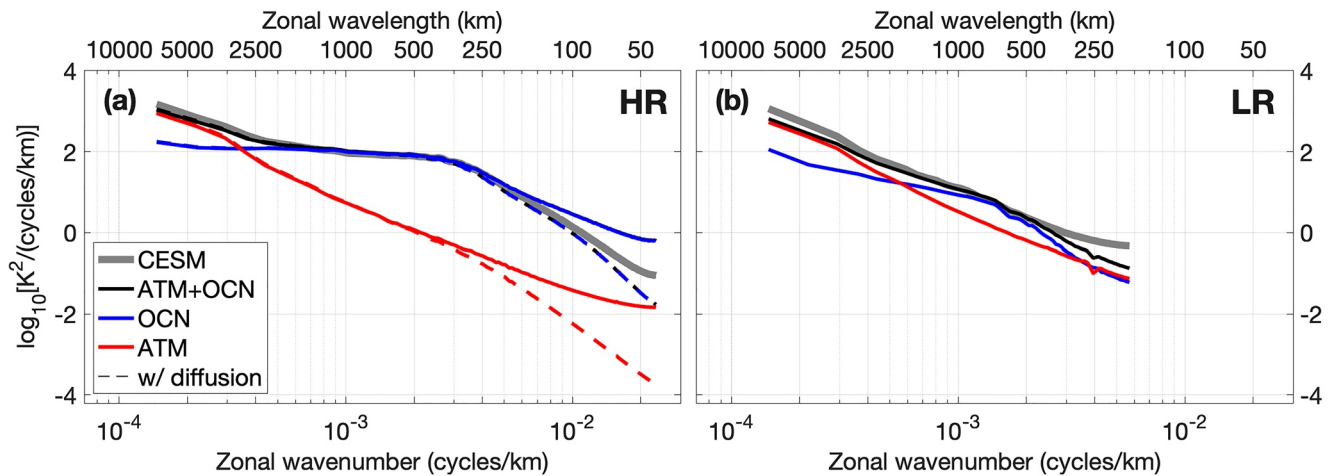


Figure 5. Stochastic model estimates of the zonal wavenumber power spectral density of sea surface temperature (SST) (G'_{TT}) for high-resolution (HR) and low-resolution (LR) (panels a and b, respectively) at 40°S in the Pacific Ocean. The panels show the ocean-driven (OCN) and atmosphere-driven (ATM) components of the stochastic model solutions (blue and red lines, respectively), and their sum (ATM + OCN, black). The continuous lines are results obtained using the stochastic model described by Equation 6, while the dashed lines denote estimates obtained using a formulation extended to include a diffusion term, assuming an eddy diffusivity coefficient equal to 100 m²/s. The thick gray lines are the reference SST spectra computed using CESM data.

significantly smaller variances in OCN, resulting in a total G'_{TT} spectrum with shape similar to that of ATM. Estimates of G'_{QQ} for both HR and LR (not shown) reveal characteristics similar to those described for G'_{TT} .

At zonal wavelengths smaller than ~300 km, G'_{TT} (Figure 5a) and G'_{QQ} (not shown) estimates for HR decay at a k^{-2} rate, in contrast with the k^{-4} rate of reference results. Nevertheless, the stochastic model solutions can reproduce the k^{-4} slope if a diffusion term [$\kappa(\partial^2 T/\partial x^2)$] is added to Equation 5 with an eddy diffusivity coefficient $\kappa = 100$ m²/s, defined empirically. The impact of including a diffusion term in corresponding LR estimates was negligible. The rationale for adding a diffusion term to the FCL98 stochastic model is further discussed in Section 4.3.

The obtained γ'_{TQ} and $|\theta'_{TQ}|$ estimates also reproduce spectral characteristics seen in the reference HR results (Figure 6) and LR results (not shown). For HR, they demonstrate that the low coherence/90° phase relationship at spatial scales larger than the atmospheric R_1 in the extratropics reflects variability in SST and THF driven by atmospheric processes, while the high coherence and near-zero phase at smaller scales reflects variability predominantly driven by ocean processes (Figures 6c–6h). In addition, γ'_{TQ} and $|\theta'_{TQ}|$ estimates that neglect the diffusion effect show coherences that remain high (~0.9) at zonal wavelengths smaller than about 300 km, while estimates that including the diffusion decay to ~0.2 values as shown by the reference results (Figure 6a). Interestingly, the diffusion term also introduces a dependence on k in the ATM component of $|\theta'_{TQ}|$ (Figure 6b). Here, the phase gradually increase from 90° at about 1,000 km to 180° near the limit of the analysis at ~50 km. It is noted that the latitudinal spectrograms in Figures 6c–6h are stochastic model solutions that include the diffusion effect.

Finally, corresponding γ'_{TQ} and $|\theta'_{TQ}|$ estimates for LR (not shown) indicate that the overall smaller coherences and wider phase angles resolved by the reference LR estimates at spatial scales smaller than the atmospheric R_1 are caused by the much weaker ocean forcing relative to HR. The sensitivity of the cross-spectral statistics predicted by the FCL98 stochastic model to the relative strength of the oceanic and atmospheric noise forcing is demonstrated and further discussed in Figures S2–S3 in Supporting Information S1. Interestingly, the stochastic model results further suggest that the slightly enhanced coherences of ~0.4 and the ~50° phase factors shown by the reference LR spectra near the equator and at the latitude of the Kuroshio and Oyashio Currents reflect a response of the air-sea coupling characteristics to the ocean dynamics resolved by LR, albeit one that is still much weaker than that implied by the HR and OBS results (Figure 4).

To summarize, this Section demonstrates that HR resolves a more realistic SST and THF power spectra and cross-spectral statistics in the zonal wavenumber domain than LR at most latitudes. It also shows that, in the extratropics, corresponding stochastic model estimates can reproduce key spectral features resolved by both HR and LR, suggesting that the stochastic model is a valid physical model for interpreting the roles of oceanic and

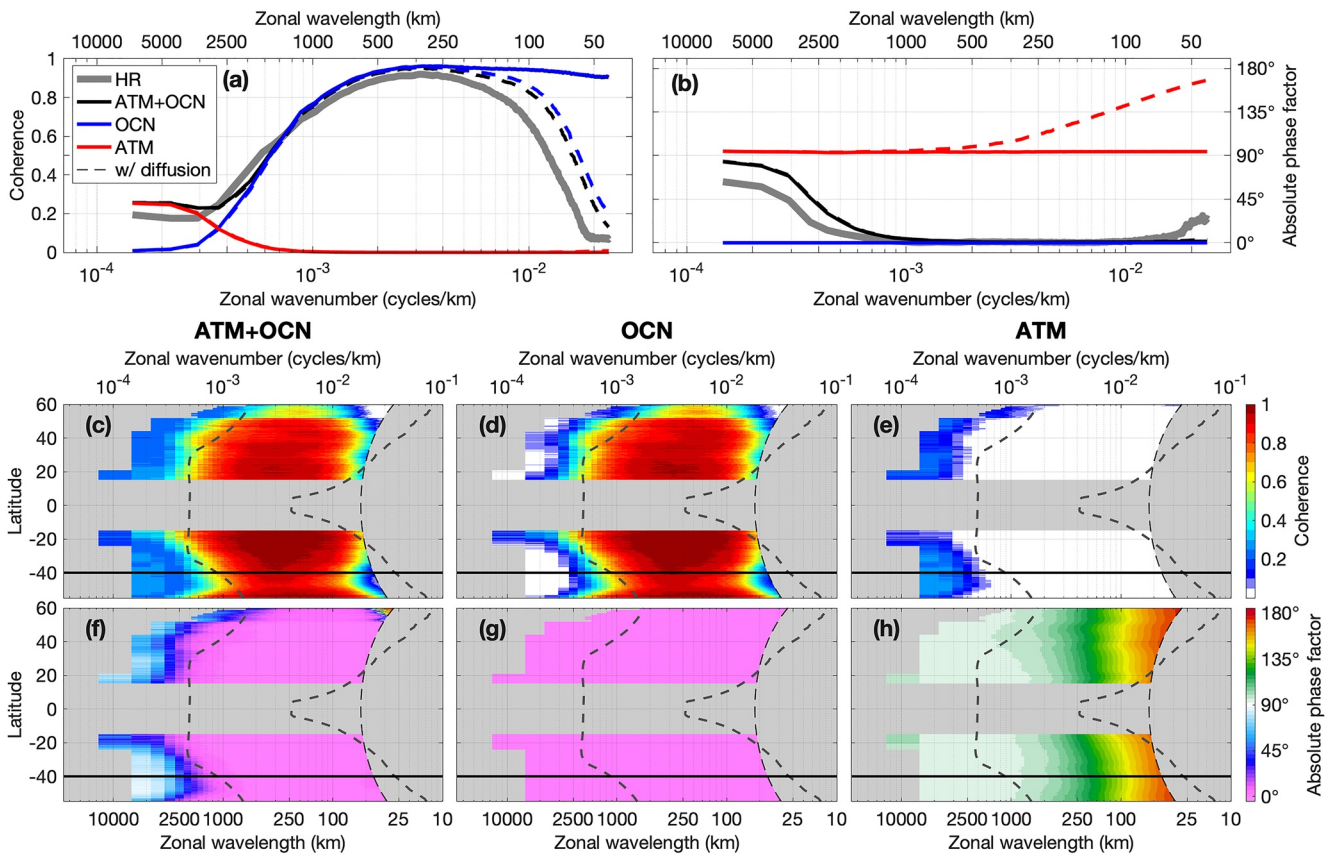


Figure 6. Stochastic model estimates of the coherence (γ_{TQ}^2) and absolute phase factor ($|\theta'_{TQ}|$) between sea surface temperature (SST) and turbulent heat flux (THF) as a function of zonal wavenumber (k) for high-resolution (HR). The top row (a–b) exemplifies the ocean and atmosphere-driven components of the stochastic model solutions (ocean-driven [OCN] and atmosphere-driven [ATM], blue and red lines, respectively), their sum (ATM + OCN, black), and the reference estimates from the HR simulations (thick gray line). The middle (c–e) and bottom (f–h) rows are latitudinal spectrograms of the ATM + OCN, OCN, and ATM components of γ_{TQ}^2 and $|\theta'_{TQ}|$, respectively. The left and right dashed lines in (c–h) represent the zonally-averaged first internal Rossby radius of deformation for the atmosphere and the ocean, respectively, the thin dashed line is the spatial Nyquist frequency for the spectral analysis, and the black horizontal line marks the 40°S latitude used to plot the results in (a–b).

atmospheric processes in their control of the spectra. In particular, these results show that the atmosphere dominates the SST and THF variability over zonal wavelengths larger than about 2,000–2,500 km. Toward smaller wavelengths, HR and OBS estimates suggest that resolved mesoscale ocean processes explain most of the SST and THF variability and co-variability over wavelengths between 100 km and the atmospheric R_1 (~ 600 – $2,000$ km), scales that are thus longer than the typical mesoscale range ($\mathcal{O}(10^1 - 10^2 \text{ km})$). Diffusion effects also become important at scales of ~ 300 km or less. The significant influence of ocean processes is seen not only at the latitudes of intense, nearly zonal extratropical current systems (such as the Kuroshio and Oyashio Currents) but also at more quiescent regions such as the subtropical gyres.

3.2.2. Frequency Spectra

This Section now examines spectral quantities computed in frequency domain for the Pacific Ocean. First, the G_{TT} estimates obtained for OBS, HR, and LR show a red spectrum shape at all analyzed latitudes (Figures 7a and 7b), although OBS and HR resolve variances larger than LR at most frequencies in the extratropics with the largest differences occurring at periods shorter than about 1,000 days (Figures 7c–7e). In turn, the G_{QQ} estimate for LR is approximately white (Figure 7f) while corresponding OBS and HR results show variance levels similar to LR at intraseasonal timescales that significantly increase relative to LR over intraseasonal to annual periods. At periods longer than annual, the G_{QQ} for HR and OBS are also approximately white (Figures 7f–7j).

To interpret the differences of G_{TT} and G_{QQ} estimates for LR relative to those obtained for HR and OBS, focus is given on 40°S as representative of their behavior in the extratropics (left panels in Figure 8). Corresponding

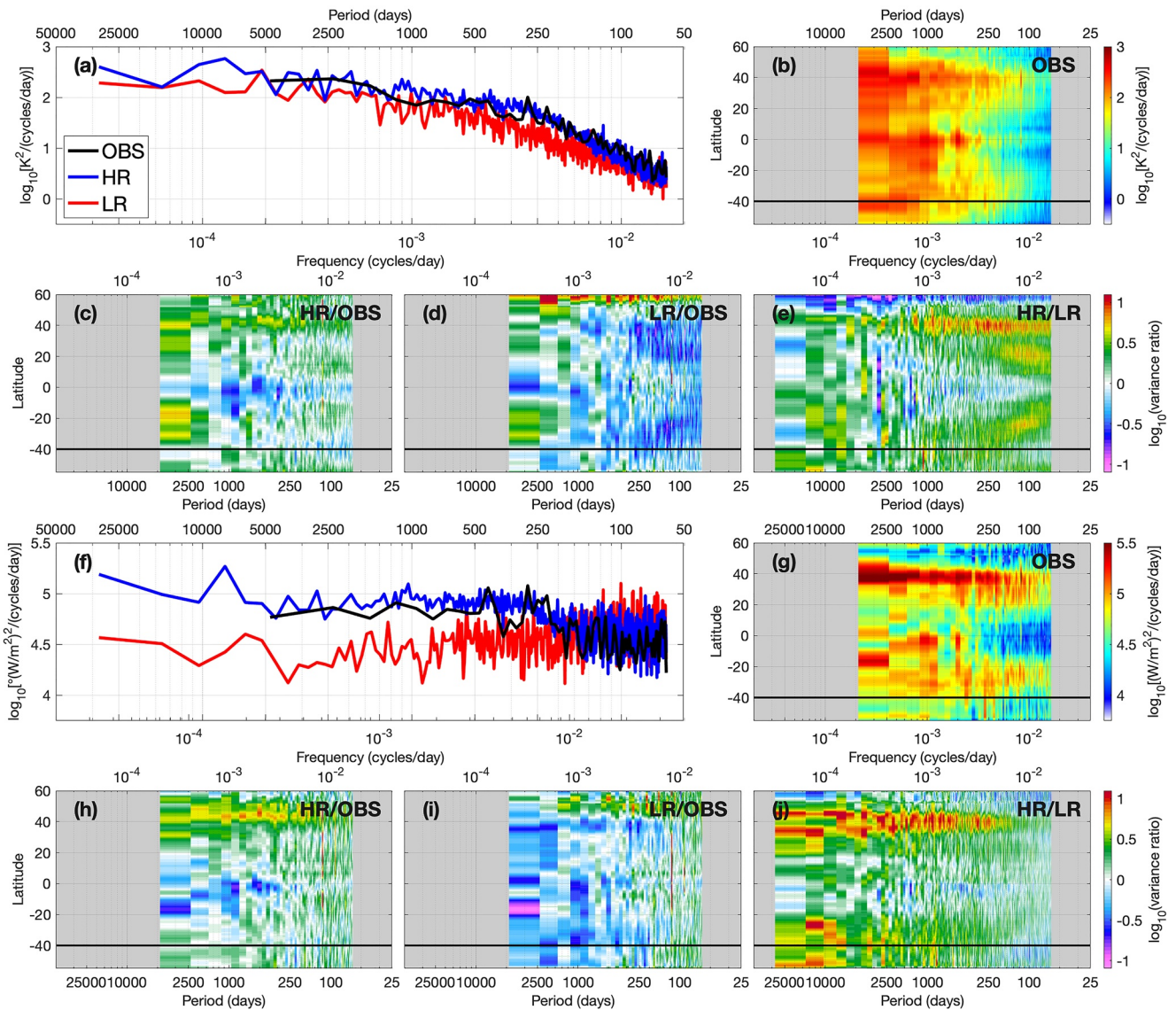


Figure 7. Power spectral density of sea surface temperature (SST) (G_{TT}) and turbulent heat flux (THF) (G_{QQ}) computed as a function of frequency for the Pacific Ocean using high-resolution (HR), low-resolution (LR), and satellite observations (OBS) data. Panel (a) show G_{TT} estimates retrieved for 40°S, (b) is the latitudinal G_{TT} spectrogram for OBS (c–d) show the ratio of the OBS estimates shown in (b) relative to the HR and LR results, and (e) the ratio between the HR and LR results. Panels (f–g) show corresponding results for G_{QQ} . The black horizontal line denotes the 40°S latitude used to plot the results in panels (a) and (f).

stochastic model results (G'_{TT} and G'_{QQ}) suggest that the larger SST and THF variances in HR relative to LR likely arise from the action of ocean processes, since the atmosphere-driven component (ATM) of the stochastic model estimates show similar shape and magnitudes for both HR and LR while the ocean-driven component (OCN) is significantly larger in HR.

Starting with G'_{TT} , the stochastic model solutions predict that oceanic and atmospheric noise both result in a red spectrum (Figures 8a and 8c). There is consensus in literature that the linear stochastic theory explains the red spectrum SST response to atmospheric forcing, whereas the present results indicates that ocean forcing induce low-frequency oscillations in SST through a similar mechanism. More specifically, the linear stochastic theory describe the low-frequency SST variability emerging in response to stochastic forcing as a first-order Markov process where, at short time-scales, the ocean acts as an integrator of the forcing noise, while at long time-scales the growth of the SST anomalies is limited by the damping action of surface turbulent heat fluxes (THF) and upper-ocean mixing (Frankignoul & Hasselmann, 1977; Hall & Manabe, 1997; Hasselmann, 1976; Patrizio &

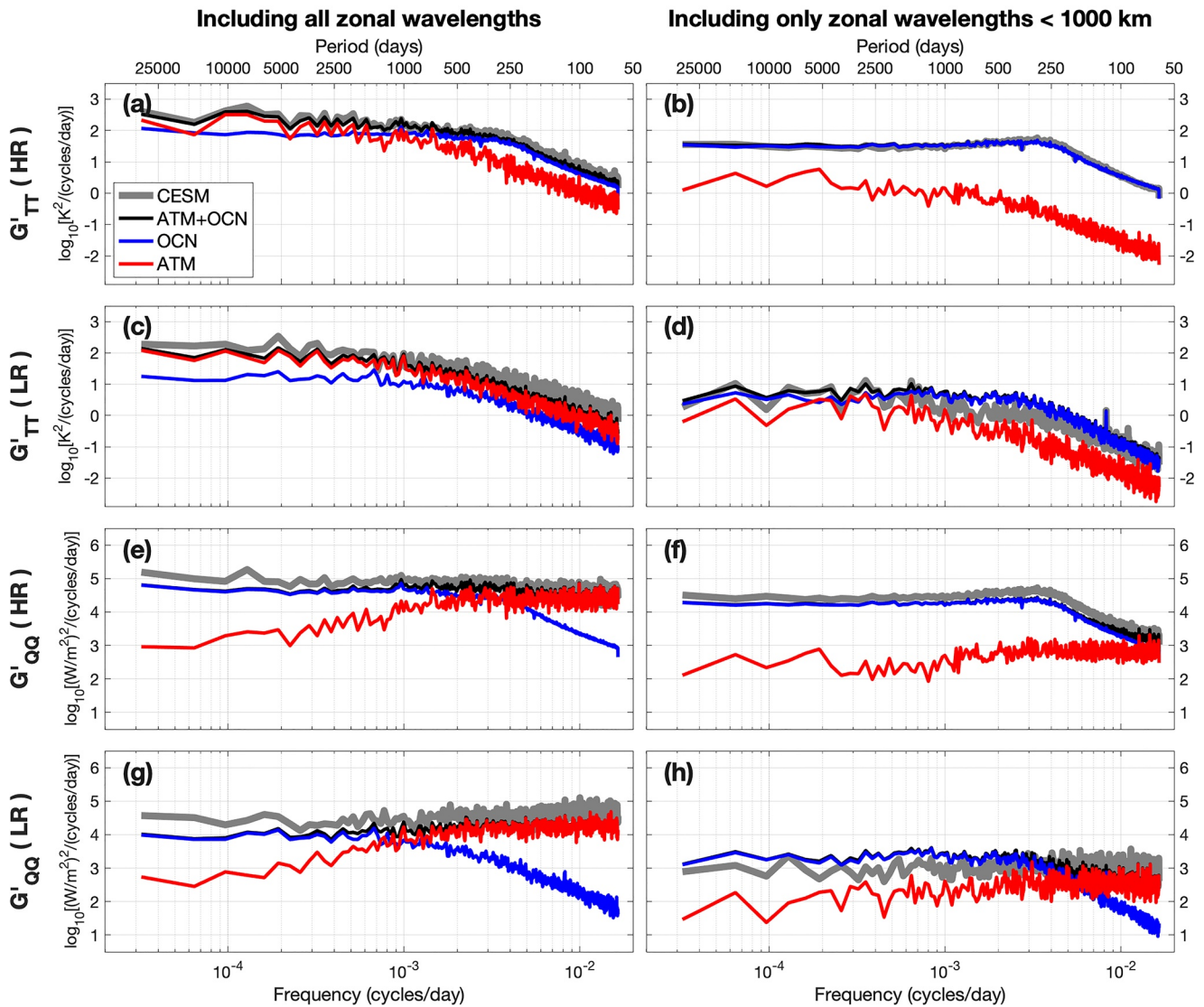


Figure 8. Stochastic model estimates of the frequency power spectrum of sea surface temperature (SST) (G'_{TT} , panels a–d) and turbulent heat flux (THF) (G'_{QQ} , e–h) for high-resolution (HR) and low-resolution (LR), illustrated for 40°S in the Pacific Ocean. The left column show estimates integrated over all zonal wavelengths, while the results in the right column are integrated over wavelengths smaller than 1,000 km. In all panels, the blue and red lines refers to the ocean and atmosphere-driven components of the stochastic model solutions (ocean-driven (OCN) and atmosphere-driven (ATM), respectively), and the black lines shows their sum (ATM + OCN). The thick gray lines show the reference SST and THF spectra from HR and LR.

Thompson, 2022). It is further noted that the ATM components of the G'_{TT} estimates are redder than their OCN components because the geophysical noise spectrum defined for the atmosphere is slightly red while for the ocean it is nearly white (cf. Figures 1c and 1d). In HR, this leads to ATM with magnitudes that are generally larger than those of OCN at periods longer than about 1,000 days, and to larger variances in OCN at shorter periods. In LR, OCN is weaker than ATM throughout.

In contrast, G'_{QQ} estimates for HR (Figure 8e) indicate that ATM accounts for most of the turbulent heat flux variability at periods shorter than 500 days while OCN is dominant at longer periods. In LR (Figure 8g), even though the ocean-driven component is much smaller than in HR, it also explains most of the THF variability over periods longer than about 1,000 days. These characteristics are explained by the ocean forcing also driving a red spectrum response in G'_{QQ} owing to the dependence of surface turbulent heat fluxes on SST, combined with the fact that atmospheric forcing results in a “blue” G'_{QQ} spectrum, where the variances decrease toward lower frequencies. Such blue spectrum response was also reported in Barsugli and Battisti (1998), which interpreted this feature as

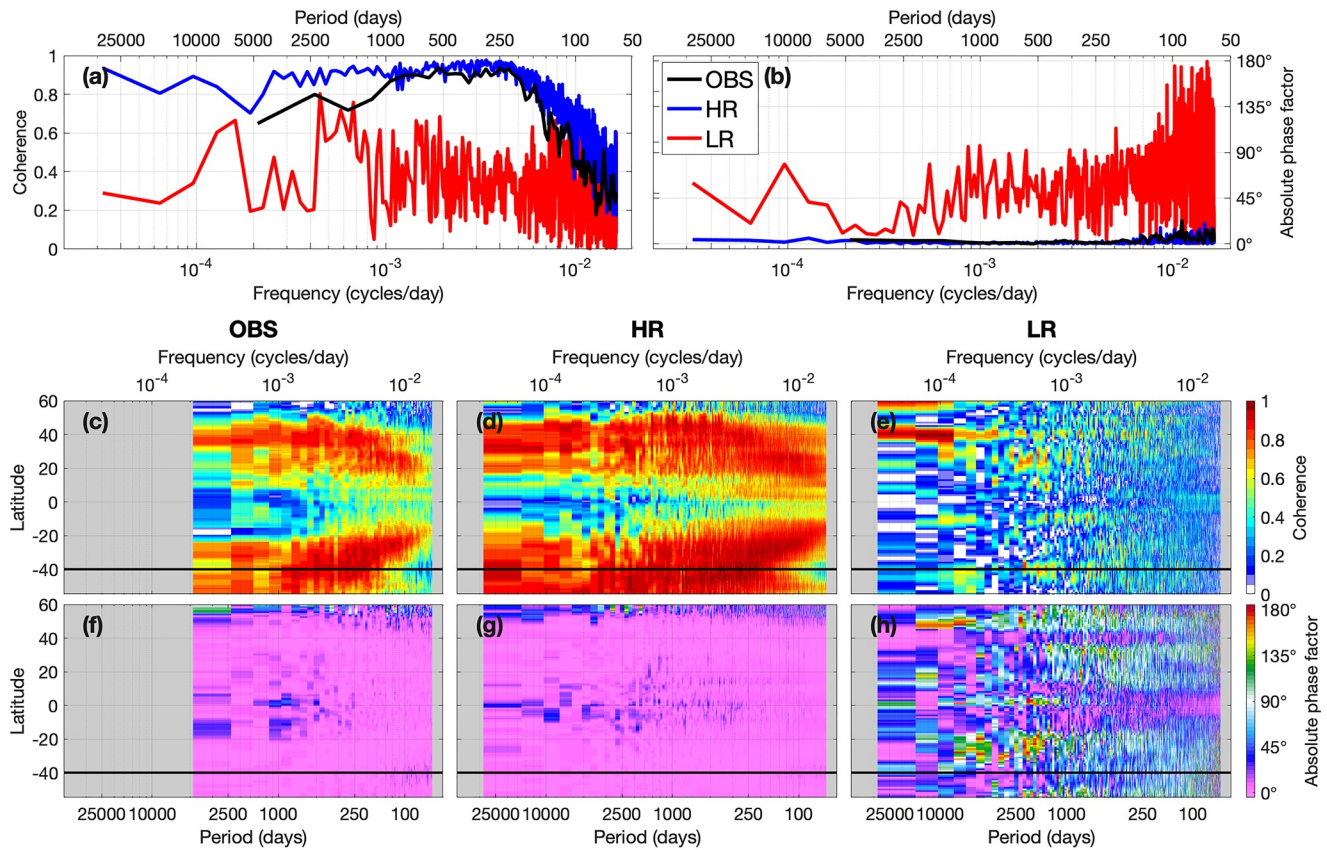


Figure 9. Similar to Figure 4, but for coherence and absolute phase factor estimates (γ_{TQ}^2 and $|\theta_{TQ}|$, respectively) computed for high-resolution (HR), low-resolution (LR), and satellite observations (OBS) as a function of frequency considering zonal wavelengths smaller than 1,000 km.

reflecting the adjustment of the ocean temperatures to the air temperatures over time, which reduced the air-sea temperature contrast and consequently the turbulent heat flux variability toward lower frequencies.

To further evaluate the importance of resolved mesoscale ocean processes in the SST and THF variability, the right panels in Figure 8 contrast the frequency-domain spectra of these quantities (G_{TT} and G_{QQ}) retrieved for both HR and LR, with their corresponding stochastic model estimates (G'_{TT} and G'_{QQ}) for zonal wavelengths smaller than 1,000 km. This isolates scales that the zonal wavenumber analysis (Section 3.2.1) suggests to be dominated by ocean processes. For HR, filtering out the large scales result in G_{TT} and G_{QQ} (Figures 8b and 8f) that are both red and similar to OBS (not shown), with corresponding stochastic model estimates indicating that OCN accounts for most of the variance of both quantities. In turn, LR estimates show significantly smaller variances in G_{TT} and G_{QQ} relative to HR and OBS, attributed by the stochastic model results to a small ocean-driven variability (Figures 8d and 8h). The SST and THF spectral responses to ocean and atmospheric forcing are further discussed in light of FCL98 stochastic model solutions in Supporting Information S1.

Next, estimates of the cross-spectral statistics coherence (γ_{TQ}^2) and absolute phase factor ($|\theta_{TQ}|$) computed for OBS and HR considering zonal wavelengths smaller than 1,000 km (Figure 9) reveal near-zero phase factors at all latitudes and over the entire frequency range, with the highest coherences (>0.4) occurring in the extratropics. The γ_{TQ}^2 for OBS and HR also indicate that enhanced values usually appear over higher frequencies toward the equator, characteristic attributed to the equatorward increase on the phase speed of oceanic Rossby waves and the propagation speed of mesoscale eddies (Laurindo et al., 2019). The high coherences also tend to persist until the lowest frequencies resolved by the analysis (Figures 9c and 9d). In LR, γ_{TQ}^2 and $|\theta_{TQ}|$ show sharp variations in frequency domain at most latitudes, although near-zero phases can be observed near the equator and at 40°N at most frequencies (Figure 9h). In addition, near-zero phase is also seen at most latitudes over periods longer than about 2,500 days.

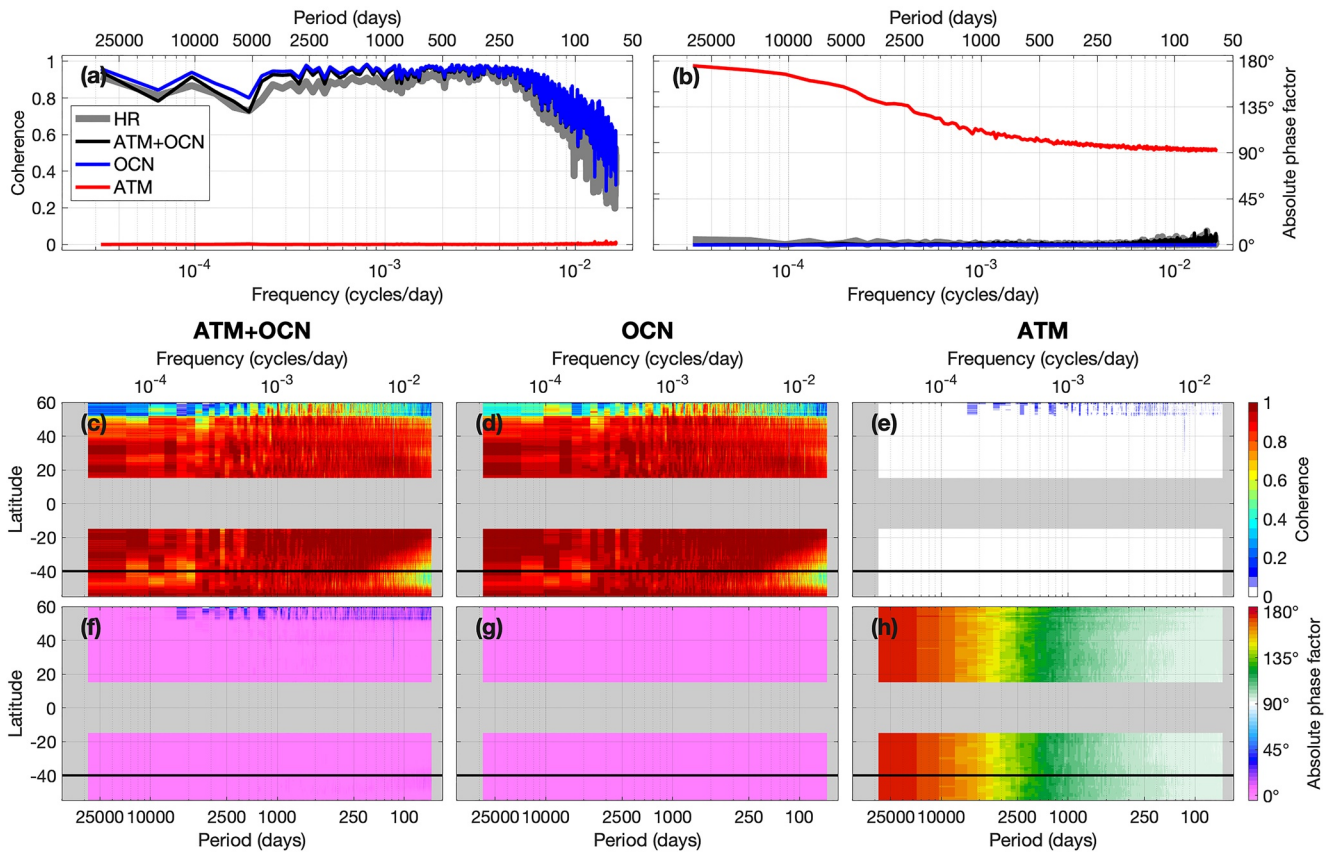


Figure 10. Similar to Figure 6, but for stochastic model estimates of coherence and absolute phase factor (γ_{TQ}^2 and $|\theta'_{TQ}|$, respectively) computed as a function of frequency considering zonal wavelengths smaller than 1,000 km.

Stochastic model estimates of coherence (γ_{TQ}^2) and absolute phase factor ($|\theta'_{TQ}|$) for HR (Figure 10) are visually similar to the OBS and HR results shown in Figure 9. Thus, in the extratropics, ocean forcing is responsible for the highly coherent and in-phase relationship between SST and THF over the entire analyzed frequency range. In support of this interpretation, estimates obtained for LR (not shown) indicate that the reduced variances in OCN leads to smaller coherence and generally larger phase relative to HR, characteristics further demonstrated in Figure S2 in Supporting Information S1. However, the stochastic model results also reveal a stronger imprint of ocean processes than implied by the results obtained using SST and THF data from OBS, HR, and LR (Figures 9e and 9h). While this suggest that the stochastic model estimates overestimate the influence of ocean processes, the cross-spectral statistics are sensitive to the amount of uncorrelated noise in the data. Due to simplified nature of the FCL98 stochastic model formulation, it is possible that the stochastic model estimates produce a larger signal-to-noise ratio than that present in the satellite observations and the HR and LR outputs.

These results indicate that, at most extratropical latitudes, the resolved ocean variability induce a red spectrum response in frequency space in both SST and THF, and that both quantities remain highly coherent and in-phase with each other over periods from 2 months until the limit at the analysis at about 80 years in HR and 13 years in OBS. The signature of ocean processes is significantly smaller in LR owing to a weaker temperature forcing by ocean processes relative to HR and OBS.

4. Discussion

4.1. Origins of the Spatial-Scale Dependency of Air-Sea Interactions

The results of the zonal wavenumber spectral analysis (Section 3.2.1) suggests that, in OBS and HR, atmospheric processes dominate the extratropical SST and THF variability and co-variability at zonal wavelengths larger than

~2,000 km while ocean processes dominate at smaller scales. Variability driven by ocean processes prevail at these scales because the atmospheric forcing spectra, while very energetic at large scales, decay toward higher wavenumbers at a steep k^{-3} rate that allows the ocean influence to become important. Supporting this interpretation, the weaker ocean forcing in LR leads to G_{TT} and G_{QQ} with shapes similar to that of the atmospheric forcing spectra.

The transition between atmosphere-to ocean-driven variability resolved by OBS and HR occurs at zonal wavelengths longer than implied by other studies. In particular, Bishop et al. (2017) computed time-domain correlations between SST tendency and THF and between SST and THF using data low-pass filtered in space using a moving average procedure (Boxcar filter), defining the transition scale as the size of the averaging window for which both pairs of quantities produce the same absolute correlations. Using satellite data, the authors obtained values smaller than 500 km in eddy-rich regions such as western boundary current systems and the ACC. The follow-up study of Small et al. (2019) investigated these relationships in an eddy-resolving climate simulation, and obtained transition scales of about 700 km at eddy-rich regions. While the differences relative to the results of the present work still need to be reconciled, they can potentially be associated with the fact that the size of the spatial averaging window does not correspond to the filter cutoff scale. This implies that the spatial filtering operation applied in these studies potentially attenuated variability over wavelengths longer than reported, thus biasing low the estimated transition scales.

The results of the present work indicate that the influence of ocean processes becomes apparent in HR and OBS at zonal wavelengths near and below the atmospheric R_1 , and the latitudinal dependence of R_1 resembles that of the scales where ocean processes start to dominate. Laurindo et al. (2019) finds a similar spatial scale dependence on the linear spectral relationship between SST and equivalent-neutral 10-m wind speed from satellite data and an eddy-resolving climate model simulation, observing negative correlations between SST and wind speed indicative of atmosphere-driven variability transitioning to positive correlations typical of ocean-driven variability also near the atmospheric R_1 . Their results relate to those of this study considering that the SST-driven anomalies in THF induce atmospheric boundary layer responses that ultimately lead to near-surface wind anomalies positively correlated with the underlying SST signal (cf. Small et al., 2008; Chelton & Xie, 2010).

The potential physical connection between the atmospheric R_1 and the transition scale from atmosphere-driven to ocean-driven SST and THF variability warrants further investigation, although one possibility can be found at the geostrophic turbulence theory of Charney (1971). The theory predicts that the kinetic energy of synoptic-scale baroclinic atmospheric systems, that scale as a function of the Rossby radius of deformation, will be transferred to smaller spatial scales at a k^{-3} rate (Charney, 1971; Lindborg, 2006; Tulloch & Smith, 2009). Indeed, the power spectra of near-surface humidity (the quantity used to represent the atmospheric forcing signal in the FCL98 stochastic model) show a meridional variation that resembles that of the atmospheric R_1 (not shown). Since the presented results indicate that the ocean-driven SST and THF variability dominates as atmospheric motions become progressively weaker toward higher wavenumbers, the variation of the transition scale between atmosphere- and ocean-driven regimes as a function of the atmospheric R_1 is potentially underpinned by a dependence of the functional structure of the spectra of atmospheric motions on the Rossby radius of deformation.

4.2. SST and THF Response to Ocean Forcing in Frequency Domain

At spatial scales smaller than 1,000 km, the SST and THF variability resolved by OBS and HR show a red spectrum structure in frequency space, with both quantities remaining highly coherent and in-phase with each other over timescales from 2 months until the limit of the analysis at about 80 years in HR and 13 years in OBS at most extratropical latitudes. Corresponding stochastic model estimates (Section 3.2.2) suggest that these features arise from a red spectrum SST response to stochastic ocean forcing analogous to that induced by the atmosphere (e.g., Frankignoul & Hasselmann, 1977; Hasselmann, 1976), that is mirrored in THF due to the dependence of this quantity on SST.

If all spatial scales are retained in the spectral analyses, the obtained results indicate that, in HR, ocean forcing prominently enhances the extratropical SST variability over periods shorter than about 500 days while atmospheric forcing dominates the variability at longer timescales, results compatible with the findings of Patrizio and Thompson (2022) and Martin et al. (2021). More specifically, Patrizio and Thompson (2022) employed a stochastic climate model formulation similar to the one used here, further accounting for a feedback term associated with

ocean dynamics computed as the 1-month lag-regression coefficient between OHFC and SST, and found that ocean processes significantly enhanced the temperature variability over periods shorter than about 2 years. The study by Martin et al. (2021), based on a frequency-space temperature variance budget analysis of an idealized, high-resolution air-sea coupled simulation of a western boundary current system analogous to the Gulf Stream, found that the ocean dynamics prominently contributes to the upper-ocean temperature variability over annual timescales and shorter. Both Patrizio and Thompson (2022) and Martin et al. (2021) found that, although ocean processes also contribute to the upper-ocean temperature variability at lower frequencies, their relative importance becomes secondary to that of atmospheric processes.

The influence of resolved mesoscale currents in the SST variability over a wide range of timescales is also consistent with the results of Sérazin et al. (2015); Sérazin et al. (2017, 2018) and Constantinou and Hogg (2021). In particular, Sérazin et al. (2015); Sérazin et al. (2018) showed that, in eddy-resolving ocean-only simulations, intrinsic ocean variability dominated the SSHA variance over spatial scales smaller than six geographical degrees over much of the extratropics at interannual to decadal timescales, also accounting for large fractions (~30%–50%) of the variance over large spatial scales (>12°) at eddy-rich regions such as the ACC and the seaward extensions of western boundary currents. Sérazin et al. (2017) and Constantinou and Hogg (2021) found a similar influence of ocean processes in the ocean heat content resolved by eddy-permitting and eddy-resolving ocean simulations.

The THF response to ocean-driven SST variability over a wide range of timescales has also been reported previously. In particular, the mixed-layer heat budget analysis of ECCO ocean state estimates by Buckley et al. (2014); Buckley et al. (2015) showed that ocean dynamics is important in setting the interannual SST and THF variability at the Gulf Stream region. In agreement with these findings, Bishop et al. (2017) showed in satellite observations that the influence of internal ocean dynamics in driving SST and THF anomalies increase toward lower frequencies in the vicinity of energetic ocean currents, a characteristic later examined by Small et al. (2019) in an eddy-resolving CESM simulation up to annual timescales. Finally, Laurindo et al. (2019) showed that satellite observations and an eddy-resolving climate simulation both resolve SST variability positively-correlated with near-surface winds over periods between 10-day and the limit of their analysis at 2.5 years at most latitudes of all three major ocean basins. The tight relationship between both quantities reflects the atmospheric boundary layer response to heat flux anomalies associated with mesoscale SST features, and was absent in outputs from a corresponding eddy-parameterized climate simulation.

4.3. Limitations of the Stochastic Model Analysis

While the FCL98 stochastic model described by Equation 6 can reproduce key characteristics of the extratropical SST and THF power spectra and cross-spectral statistics, it is an idealized formulation that does not represent important processes involved in thermodynamic air-sea interactions. This Section discusses such limitations and those emerging from other assumptions of the presented analysis.

First, the FCL98 stochastic model does not account for the atmospheric adjustment to SST, a process that is represented by the stochastic, coupled ocean-atmosphere energy balance model proposed by Barsugli and Battisti (1998) (hereafter BB98) employed by previous studies (Bishop et al., 2017; Sun & Wu, 2021; Sura & Newman, 2008; Wu et al., 2006). However, tests with the BB98 formulation showed that obtaining SST power spectra with magnitudes comparable to those resolved by HR and LR produced THF power spectra that was too small by about two orders of magnitude. This issue potentially reflects the ocean and atmosphere becoming too strongly coupled to each other in the BB98 model, reducing the air-sea temperature contrast and consequently the THF variability. Conversely, the FCL98 model produced SST and THF power spectra with magnitudes comparable to those resolved by HR and LR.

Within the framework of FCL98, atmospheric processes solely modulates THF through stochastic variability in near-surface atmospheric temperature. This approach neglects various mechanisms through which internal atmospheric processes can affect SST and THF, including:

1. The role of the atmosphere in generating Ekman currents, which are significant contributors to OHFC and consequently to the SST variability at large spatial scales (Larson et al., 2018; Small et al., 2020) and at long time-scales (Martin et al., 2021). This implies that using OHFC to represent the ocean noise forcing overestimates the role of ocean processes for driving the SST and THF variability at these scales.

2. The influence of stochastic fluctuations in surface wind speed, which drives significant fractions of the THF variability (e.g., Alexander & Penland, 1996; Frankignoul et al., 1998; Lee et al., 2008; Proistosescu et al., 2018; Sura et al., 2006). Accounting for this effect would likely affect the frequency-domain SST and THF response to atmospheric forcing, potentially leading to a larger influence of atmospheric motions on lower frequencies than implied by current results (e.g., Sura et al., 2006; Sura & Sardeshmukh, 2009).
3. Radiative forcing associated with stochastic cloud variability, a process known to induce SST anomalies negatively correlated with cloud cover at seasonal timescales (e.g., Alexander et al., 2006; Park et al., 2006; Proistosescu et al., 2018; Spencer & Braswell, 2010).

Moreover, the FCL98 formulation does not represent the influence of nonlocal processes such as ENSO teleconnections that are known to drive significant SST and THF variability throughout the Pacific Ocean (e.g., Alexander et al., 2002; Martinez-Villalobos et al., 2019; Park et al., 2006). It also does not account for the influence of the Pacific Decadal Oscillation (Chang et al., 2020), of modifications in the atmospheric boundary layer driven by mesoscale SST anomalies (cf. Small et al., 2008; Chelton & Xie, 2010), and of complex interactions between mesoscale SST features associated with the Kuroshio and Oyashio Currents with the tropical ocean, midlatitude storm tracks, and low-frequency climate modes (e.g., Joh et al., 2021; Ma et al., 2015; Ma et al., 2017; Siqueira et al., 2021).

This study further assumes that the mixed-layer depth h , the turbulent heat flux feedback factor λ_q , and the radiative feedback factor λ_r —quantities used to compute the coefficients α and β of Equation 6, are constant throughout the extratropics. However, the feedback factors vary strongly as a function of geographical location, season, and of the underlying mesoscale ocean dynamics (e.g., Frankignoul et al., 1998; Frankignoul & Kestenare, 2002; Park et al., 2005; Patrizio & Thompson, 2022; Smirnov et al., 2014). In addition, the mixed-layer depth is highly inhomogeneous across the global ocean and show strong seasonality at middle to high latitudes. These characteristics influence the local mixed-layer heat capacity and the rates that SST anomalies are attenuated over time, and as a result they also impact the low-frequency SST variability response to stochastic forcing (e.g., Alexander & Deser, 1995; Deser et al., 2003; Dommenges & Latif, 2002). Here, the fact that the magnitudes of the atmospheric and oceanic forcing spectra are estimated by least-squares fitting the stochastic model solutions to the SST and THF spectra resolved by HR and LR (Appendix A) partially offsets errors due to the use of constant coefficients. However, as discussed in Supporting Information S1, the FCL98 stochastic model coefficients control the shape of the SST and THF frequency spectra, and setting constant values to them likely increases the misfit between the stochastic model solutions and the reference CESM estimates.

The FCL98 stochastic model described by Equation 6 also neglects the influence of upper-ocean mixing, which modulate seasonal changes in the mixed layer depth (Alexander & Deser, 1995; Deser et al., 2003; Dommenges & Latif, 2002; Park et al., 2006) and limit the growth of SST anomalies over time (Dommenges & Latif, 2002; Hall & Manabe, 1997; Park et al., 2006; Patrizio & Thompson, 2022). Here, an attempt to access the influence of mixing processes in the variability was made by adding a diffusion term to the model formulation representing the action of down-gradient eddy fluxes by mesoscale currents (cf. Section 3.2.1). Assuming an eddy diffusivity coefficient $\kappa = 100 \text{ m}^2/\text{s}$, the stochastic model estimates of the SST and THF power spectra reproduces the approximate k^{-4} slope at wavelengths smaller than 300 km shown by estimates from HR and OBS (Figure 5). Without diffusion, the stochastic model results instead decay at a slower k^{-2} rate, reflecting the spectra of the OHFC data used to represent the ocean noise forcing. This in principle suggests that diffusion influences the air-sea coupling characteristics at high wavenumbers. However, the used κ value is about one order of magnitude smaller than observational measurements (e.g., Koszalka et al., 2011; Mariano et al., 2016; Peng et al., 2015; Zhurbas et al., 2014), an underestimation that potentially stems from the idealized nature of the FCL98 formulation. On the flip side, high-resolution satellite SST data resolve a k^{-2} slope at scales smaller than 500 km (Chin et al., 2017) that is curiously similar to that of stochastic model estimates without the diffusion effect. This raises the possibility that the k^{-4} slope shown by OBS and HR reflect mapping biases and/or resolution issues rather than actual geophysical characteristics (Chin et al., 2017).

Finally, the fact that this study defines the geophysical noise forcing using OHFC and 2-m humidity data from the coupled HR and LR simulations implies that the atmospheric forcing spectrum is modified by feedbacks from the ocean and vice-versa. This can confound the interpretation of the drivers of the observed SST and THF variability. In particular, Barsugli and Battisti (1998) found that the air-sea coupling enhances the low-frequency

air temperature variance and hence the near-surface humidity, thus potentially explaining why the geophysical forcing spectrum retrieved for the atmosphere is slightly red rather than white in frequency space (Figure 1d). In addition, the forcing spectra for both mediums also include variability induced by nonlocal effects and air-sea interactions. To elucidate the role of intrinsic variability in each medium in the absence of feedbacks arising from the coupling, the presented stochastic model analysis can potentially be improved by defining the geophysical noise spectra using data from ocean-only and atmosphere-only general circulation model simulations forced by seasonal climatologies, rather than using data from the coupled HR and LR.

5. Summary and Conclusions

This work examines the SST and THF power spectra and cross-spectral statistics resolved by the J-OFURO3 observational product (OBS) and by multi-century climate model simulations run at eddy-parameterized and eddy-resolving ocean resolutions (LR and HR, respectively). These quantities are computed for the Pacific between 55°S and 60°N, over zonal wavelengths between ~50 and 10,000 km and periods from two months to 13 years using OBS and 80 years using model data. The roles of atmospheric and oceanic processes in conditioning the spectral characteristics in the extratropics are interpreted using a stochastic model of the upper-ocean temperature evolution forced by noise terms representing the action of intrinsic variability in both mediums. Here, the noise terms are defined using actual geophysical data from HR and LR to simulate realistic variance distributions in spectral space.

Spectral estimates obtained as a function of zonal wavenumber indicate that, at most latitudes, all datasets resolve similar SST and THF variability at wavelengths larger than 2,500 km. However, toward smaller spatial scales, their variances in HR and OBS increase relative to LR, with the most significant differences (one order of magnitude or more) found at zonal wavelengths near and smaller than the atmospheric first internal Rossby deformation radius (R_1). At these scales, SST and THF variability are highly related to each other in HR and OBS but not in LR. The corresponding stochastic model results indicate that the large-scale SST and THF variability is predominantly driven by the atmosphere and that the tight relationship between both quantities toward higher wavenumbers in HR and OBS arise from the action of ocean processes. This relationship is virtually absent in LR due to the much weaker ocean forcing relative to HR.

The stochastic model analysis further suggest that the transition from atmosphere-driven variability to ocean-driven in HR and OBS occurs owing to the steep k^{-3} decay of the atmosphere noise spectrum. This characteristic, combined with the approximately constant (white) ocean noise spectra from the largest resolvable wavelengths until ~300 km, allows the ocean-forced SST and THF variability to become larger than that forced by the atmosphere at scales below ~2,000 km. It is hypothesized that the similar meridional variation of the transition scale with that of the atmospheric R_1 reflects the dependence of atmospheric motions' power spectrum on the Rossby radius.

Spectral quantities computed as a function of frequency show that OBS and HR has larger SST variances than LR at most frequencies in the extratropics, most prominently over periods shorter than about 1,000 days. In contrast, THF variability is enhanced in OBS and HR relative to LR over annual periods and longer. Isolating zonal wavelengths smaller than 1,000 km, HR and OBS reveal a red SST and THF power spectra (with more power over lower frequencies), with corresponding cross-spectral statistics indicating that these quantities are highly related to each other at all timescales. Corresponding stochastic model estimates suggest that these characteristics arise from the action of ocean processes. The observed red spectral response in SST to ocean forcing is analogous to that induced by stochastic atmospheric variability, where the ocean integrates the noise to induce low-frequency oscillations. This red spectrum response is also seen in THF due to the dependence of this quantity on SST. It is noted that the linear stochastic theory describes the low-frequency variability emerging in response to internal oceanic and atmospheric noise forcing as a first-order Markov process, being thus unpredictable in principle. However, the results of the present study do not rule out the existence of predictable forms of variability in the ocean or the atmosphere that are intrinsic to either medium or that arise from their coupling.

These results support the conclusion that climate models with eddy-resolving oceans resolve more realistic air-sea coupling characteristics than their eddy-parameterized counterparts. In particular, they indicate that resolved mesoscale ocean phenomena can modulate a significant fraction of the extratropical SST and THF variability over a wide range of spatial scales ($\mathcal{O}(10^1 - 10^3 \text{ km})$) and from intraseasonal to multidecadal timescales. It is

reminded that HR and LR also show distinct horizontal resolutions in the atmosphere (0.25° vs. 1°) that enable a better representation of phenomena such as weather fronts in HR. While our results suggest that the main differences between the simulations can be traced back to mesoscale ocean processes, they do not rule out a potential influence of the higher atmospheric resolution in HR on the resolved SST and THF variability.

Finally, it is noted that, while stochastic models can be used to infer the roles of the atmosphere and ocean in driving SST and THF variability, these idealized systems cannot represent all the physical complexity of the processes involved in the thermodynamic air-sea interactions, nor inform about the nature of the phenomena in both mediums responsible for the generation and dissipation of SST anomalies. With this in mind, a potential follow-on investigation involves using spectral methods to examine the key terms in the upper-ocean heat balance equation and in the turbulent heat flux bulk formulations responsible for maintaining the SST and THF variability over different spatial scales (in both zonal and meridional directions) and temporal scales across the global ocean, as resolved by high-resolution climate models. Considering the well-known dispersion characteristics of oceanic and atmospheric phenomena, further insight on their roles in the variability could also be gained by distinguishing the contributions of eastward and westward-propagating signals in space-time spectral analyses.

Appendix A: Estimating the Geophysical Noise Spectra

To compute the geophysical noise $\langle |\tilde{N}_o|^2 \rangle$ and $\langle |\tilde{N}_a|^2 \rangle$, zonal-temporal data series of OHFC and 2-m humidity are first selected at each latitude within the Pacific basin mask (Figure 2h). These data series have their means removed along both zonal and temporal directions. A best-fit model composed of a linear temporal trend and of annual and semiannual harmonics representing seasonal variations is also removed. The remaining anomaly data series are then normalized by their own standard deviations to make them non-dimensional and with variances equal to one.

The normalized data series are then windowed in 80-year segments that overlap each other by 50% in the temporal domain, which results in a total of three segments for HR and 11 for LR at a given latitude. To increase the data available for the analysis, subsequent calculations uses data obtained within 2° of each latitude—that is, estimates for 10°N are computed using data from between 8° and 12°N. This procedure results in 48 data segments for HR and 44 for LR at each latitude.

Each zonal-temporal data series segment is then Fourier transformed to the zonal wavenumber and frequency domains. These are referred to as $\tilde{M}_{o,j}(k, \omega)$ and $\tilde{M}_{a,j}(k, \omega)$ for the ocean and atmosphere, respectively, where $j = 1, 2, 3, \dots, n_j$ lists the j th realization of the spectra of a total of n_j realizations. They are related to the geophysical noise spectra as:

$$\langle |\tilde{N}_o(k, \omega)|^2 \rangle = \langle |\tilde{M}_o(k, \omega)|^2 \rangle \sigma_o^2, \quad (\text{A1})$$

$$\langle |\tilde{N}_a(k, \omega)|^2 \rangle = \langle |\tilde{M}_a(k, \omega)|^2 \rangle \sigma_a^2. \quad (\text{A2})$$

Here, the brackets denote an ensemble average over the n_j realizations, while σ_o^2 and σ_a^2 are the variances that the geophysical noise $\langle |\tilde{N}_o|^2 \rangle$ and $\langle |\tilde{N}_a|^2 \rangle$ should integrate to for approximating stochastic model solutions defined by Equations 7 and 8 to the SST and THF power spectra resolved by HR and LR.

To estimate σ_o^2 and σ_a^2 , the SST and THF power spectra resolved by HR and LR (Equations 1 and 2) are equaled to the analytical solutions for the upper-ocean temperature and surface heat flux power spectra derived from the FCL98 stochastic model (Equations 7 and 8). Further using Equations A1 and A2, the following relations can be obtained:

$$|\tilde{T}_j(k, \omega)|^2 = \left[\frac{v^2 |\tilde{M}_{o,j}(k, \omega)|^2}{4\pi^2 \omega^2 + (\alpha + \beta)^2} \right] \sigma_o^2 + \left[\frac{\alpha^2 |\tilde{M}_{a,j}(k, \omega)|^2}{4\pi^2 \omega^2 + (\alpha + \beta)^2} \right] \sigma_a^2 + \text{residuals}, \quad (\text{A3})$$

$$|\tilde{Q}_j(k, \omega)|^2 = \left[\frac{\lambda_q^2 v^2 |\tilde{M}_{o,j}(k, \omega)|^2}{4\pi^2 \omega^2 + (\alpha + \beta)^2} \right] \sigma_o^2 + \left[\frac{\lambda_q^2 (4\pi^2 \omega^2 + \beta^2) |\tilde{M}_{a,j}(k, \omega)|^2}{4\pi^2 \omega^2 + (\alpha + \beta)^2} \right] \sigma_a^2 + \text{residuals}. \quad (\text{A4})$$

Since \tilde{T}_j , \tilde{Q}_j , $M_{o,j}$, and $\tilde{M}_{a,j}$ are known, σ_o^2 and σ_a^2 can be estimated via least squares. Prior to the fitting operation, the order j of the spectral realizations is randomized without replacement (i.e., shuffled) to reduce correlations arising the zonal and temporal coincidence of the data.

Considering n_k (n_ω) as the number of discrete coordinates in the zonal wavenumber (frequency) domain (A3) and (A4) are then redefined as a system with $n = 2n_k n_\omega n_j$ linear equations, as:

$$y_i = A_i \sigma_o^2 + B_i \sigma_a^2, \quad (\text{A5})$$

where $i = 1, 2, 3, \dots, n$. Here, y_i holds the $|\tilde{T}_j(k, \omega)|^2$ and $|\tilde{Q}_j(k, \omega)|^2$ estimates, A_i and B_i represents the terms enclosed by square brackets in Equations A3 and A4, and σ_o^2 and σ_a^2 are the unknowns of the system.

In matrix form (A5) can be rewritten as $y = Mz$, where M is an $n \times 2$ matrix containing the A and B vectors, and z is an 2×1 column vector with the unknowns σ_o^2 and σ_a^2 . A least-squares solution for z can then be computed as:

$$z = (M^T M)^{-1} (M^T y), \quad (\text{A6})$$

where the superscript “T” denotes transposed matrices. The estimated variances are then used to compute the geophysical noise ($|\tilde{N}_o|^2$) and ($|\tilde{N}_a|^2$) via Equations A1 and A2).

Data Availability Statement

The outputs from the HR and LR climate model simulations used in the present study are thoroughly described in Chang et al. (2020), and can be obtained from iHESP at https://ihesp.github.io/archive/products/ds_archive/Sunway_Runs.html. The J-OFURO3 data (Tomita et al., 2019) can be obtained at <https://j-ofuro.isee.nagoya-u.ac.jp/en/dataset/entry-323.html>. The Chelton et al. (1998) global climatology of the oceanic first internal Rossby radius of deformation (R_1) is available at https://ceoas.oregonstate.edu/rossby_radius. Lastly, the NCEP reanalysis model data (Kalnay et al., 1996) used to compute the atmospheric R_1 is available at <https://psl.noaa.gov/data/gridded/data.ncep.reanalysis.html>.

Acknowledgments

This research was supported in part by the National Center for Atmospheric Research (NCAR), which is a major facility sponsored by the National Science Foundation (NSF) under Cooperative Agreement No. 1852977; and in part by the International Laboratory for High Resolution Earth System Prediction (iHESP), a collaboration between the Qingdao National Laboratory for Marine Science and Technology (QNLMT), Texas A&M University (TAMU), and NCAR. L. Siqueira and B. Kirtman acknowledge support from NSF (OCE1419569, OCE1559151), the National Oceanic and Atmospheric Administration (NOAA, NA18OAR4310293, NA15OAR4320064), and the U.S. Department of Energy (DOE, DE-SC0019433). P. Chang acknowledges support from NSF (AGS1462127), NOAA (NA20OAR4310409), and DOE (DE-SC0020072). The data analyses performed for this study were carried out using computing resources provided by the Texas A&M High Performance Research Computing and the Climate Simulation Laboratory at NCAR's Computational and Information Systems Laboratory. L. Laurindo, R. Small, and F. Bryan gratefully acknowledge Stuart Bishop, Casey Patrizio, and Yiming Guo for valuable discussions throughout the development of this work. All authors thank Claude Frankignoul for his feedback on an early version of this manuscript. They also thank Joseph Barsugli and two anonymous reviewers for their thoughtful and constructive comments during peer review.

References

- Alexander, M. A., Bladé, I., Newman, M., Lanzante, J. R., Lau, N.-C., & Scott, J. D. (2002). The atmospheric bridge: The influence of ENSO teleconnections on air–sea interaction over the global oceans. *Journal of Climate*, *15*(16), 2205–2231. [https://doi.org/10.1175/1520-0442\(2002\)015<2205:TABTIO>2.0.CO;2](https://doi.org/10.1175/1520-0442(2002)015<2205:TABTIO>2.0.CO;2)
- Alexander, M. A., & Deser, C. (1995). A mechanism for the recurrence of wintertime midlatitude SST anomalies. *Journal of Physical Oceanography*, *25*(1), 122–137. [https://doi.org/10.1175/1520-0485\(1995\)025<0122:AMFTRO>2.0.CO;2](https://doi.org/10.1175/1520-0485(1995)025<0122:AMFTRO>2.0.CO;2)
- Alexander, M. A., & Penland, C. (1996). Variability in a mixed layer ocean model driven by stochastic atmospheric forcing. *Journal of Climate*, *9*(10), 2424–2442. [https://doi.org/10.1175/1520-0442\(1996\)009<2424:VIAMLO>2.0.CO;2](https://doi.org/10.1175/1520-0442(1996)009<2424:VIAMLO>2.0.CO;2)
- Alexander, M. A., Yin, J., Branstator, G., Capotondi, A., Cassou, C., Cullather, R., et al. (2006). Extratropical atmosphere–ocean variability in CCSM3. *Journal of Climate*, *19*(11), 2496–2525. <https://doi.org/10.1175/JCLI3743.1>
- Barsugli, J. J., & Battisti, D. S. (1998). The basic effects of atmosphere–ocean thermal coupling on midlatitude variability. *Journal of the Atmospheric Sciences*, *55*(4), 477–493. [https://doi.org/10.1175/1520-0469\(1998\)055<0477:TBEAO>2.0.CO;2](https://doi.org/10.1175/1520-0469(1998)055<0477:TBEAO>2.0.CO;2)
- Bendat, J. S., & Piersol, A. G. (1986). *Random data: Analysis and measurement procedures*, 3rd edn., (p. 594). John Wiley & Sons, Inc. (pp.) <https://doi.org/10.1002/9781118032428>
- Berloff, P., & Kamenkovich, I. (2013a). On the spectral analysis of mesoscale eddies. Part I: Linear analysis. *Journal of Physical Oceanography*, *43*(12), 2505–2527. <https://doi.org/10.1175/JPO-D-12-0232.1>
- Berloff, P., & Kamenkovich, I. (2013b). On the spectral analysis of mesoscale eddies. Part II: Nonlinear analysis. *Journal of Physical Oceanography*, *43*(12), 2528–2544. <https://doi.org/10.1175/JPO-D-12-0233.1>
- Bishop, S. P., Small, R. J., Bryan, F. O., & Tomas, R. A. (2017). Scale dependence of midlatitude air–sea interaction. *Journal of Climate*, *30*(20), 8207–8221. <https://doi.org/10.1175/JCLI-D-17-0159.1>
- Buckley, M. W., Ponte, R. M., Forget, G., & Heimbach, P. (2014). Low-Frequency SST and upper-ocean heat content variability in the North Atlantic. *Journal of Climate*, *27*(13), 4996–5018. <https://doi.org/10.1175/JCLI-D-13-00316.1>
- Buckley, M. W., Ponte, R. M., Forget, G., & Heimbach, P. (2015). Determining the origins of advective heat transport convergence variability in the North Atlantic. *Journal of Climate*, *28*(10), 3943–3956. <https://doi.org/10.1175/JCLI-D-14-00579.1>
- Callies, J., Ferrari, R., & Bühler, O. (2014). Transition from geostrophic turbulence to inertia–gravity waves in the atmospheric energy spectrum. *Proceedings of the National Academy of Sciences of the United States of America*, *111*(48), 17033–17038. <https://doi.org/10.1073/pnas.1410772111>
- Chang, P., Zhang, S., Danabasoglu, G., Yeager, S. G., Fu, H., Wang, H., et al. (2020). An unprecedented set of high-resolution Earth system simulations for understanding multiscale interactions in climate variability and change. *Journal of Advances in Modeling Earth Systems*, *12*(12), e2020MS002298. <https://doi.org/10.1029/2020MS002298>
- Charney, J. G. (1971). Geostrophic turbulence. *Journal of the Atmospheric Sciences*, *28*(6), 1087–1095. [https://doi.org/10.1175/1520-0469\(1971\)028<1087:GT>2.0.CO;2](https://doi.org/10.1175/1520-0469(1971)028<1087:GT>2.0.CO;2)

- Chelton, D. B., de Szoeke, R. A., Schlax, M. G., Naggar, K. E., & Siwertz, N. (1998). Geographical variability of the first baroclinic Rossby radius of deformation. *Journal of Physical Oceanography*, 28(3), 433–460. [https://doi.org/10.1175/1520-0485\(1998\)028<0433:GVOTFB>2.0.CO;2](https://doi.org/10.1175/1520-0485(1998)028<0433:GVOTFB>2.0.CO;2)
- Chelton, D. B., Gaube, P., Schlax, M. G., Early, J. J., & Samelson, R. M. (2011). The influence of nonlinear mesoscale eddies on near-surface oceanic chlorophyll. *Science*, 334(6054), 328–332. <https://doi.org/10.1126/science.1208897>
- Chelton, D. B., Schlax, M. G., Freilich, M. H., & Milliff, R. F. (2004). Satellite measurements reveal persistent small-scale features in ocean winds. *Science*, 303(5660), 978–983. <https://doi.org/10.1126/science.1091901>
- Chelton, D. B., Schlax, M. G., & Samelson, R. M. (2011). Global observation of nonlinear mesoscale eddies. *Progress in Oceanography*, 91(2), 167–216. <https://doi.org/10.1016/j.pocean.2011.01.002>
- Chelton, D. B., & Xie, S.-P. (2010). Coupled ocean-atmosphere interaction at the oceanic mesoscale. *Oceanography*, 23(4), 52–62. <https://doi.org/10.5670/oceanog.2010.05>
- Chin, T. M., Vazquez-Cuervo, J., & Armstrong, E. M. (2017). A multi-scale high-resolution analysis of global sea surface temperature. *Remote Sensing of Environment*, 200, 154–169. <https://doi.org/10.1016/j.rse.2017.07.029>
- Cho, J. Y. N., Zhu, Y., Newell, R. E., Anderson, B. E., Barrick, J. D., Gregory, G. L., et al. (1999). Horizontal wavenumber spectra of winds, temperature, and trace gases during the Pacific exploratory missions: 1. Climatology. *Journal of Geophysical Research*, 104(D5), 5697–5716. <https://doi.org/10.1029/98JD01825>
- Clement, A., Bellomo, K., Murphy, L. N., Cane, M. A., Mauritsen, T., Rädcl, G., & Stevens, B. (2015). The Atlantic Multidecadal Oscillation without a role for ocean circulation. *Science*, 350(6258), 320–324. <https://doi.org/10.1126/science.aab3980>
- Constantinou, N. C., & Hogg, A. M. (2021). Intrinsic oceanic decadal variability of upper-ocean heat content. *Journal of Climate*, 1–41. (published online). <https://doi.org/10.1175/JCLI-D-20-0962.1>
- Danabasoglu, G., Bates, S. C., Briegleb, B. P., Jayne, S. R., Jochum, M., Large, W. G., et al. (2012). The CCSM4 ocean component. *Journal of Climate*, 25(5), 1361–1389. <https://doi.org/10.1175/JCLI-D-11-00091.1>
- Deser, C., Alexander, M. A., & Timlin, M. S. (2003). Understanding the persistence of sea surface temperature anomalies in midlatitudes. *Journal of Climate*, 16(1), 57–72. [https://doi.org/10.1175/1520-0442\(2003\)016<0057:UTPOSS>2.0.CO;2](https://doi.org/10.1175/1520-0442(2003)016<0057:UTPOSS>2.0.CO;2)
- Deser, C., & Phillips, A. S. (2021). Defining the internal component of Atlantic Multidecadal variability in a changing climate. *Geophysical Research Letters*, 48(22), e2021GL095023. <https://doi.org/10.1029/2021GL095023>
- Dommenget, D., & Latif, M. (2002). Analysis of observed and simulated SST spectra in the midlatitudes. *Climate Dynamics*, 19(3–4), 277–288. <https://doi.org/10.1007/s00382-002-0229-9>
- Ducet, N., Le Traon, P.-Y., & Reverdin, G. (2000). Global high-resolution mapping of ocean circulation from TOPEX/Poseidon and ERS-1 and -2. *Journal of Geophysical Research*, 105(C8), 19477–19498. <https://doi.org/10.1029/2000JC90006>
- Early, J. J., Samelson, R. M., & Chelton, D. B. (2011). The evolution and propagation of quasigeostrophic ocean eddies. *Journal of Physical Oceanography*, 41(8), 1535–1555. <https://doi.org/10.1175/2011JPO4601.1>
- Fairall, C. W., Bradley, E. F., Hare, J. E., Grachev, A. A., & Edson, J. B. (2003). Bulk parameterization of air-sea fluxes: Updates and verification for the COARE algorithm. *Journal of Climate*, 16(4), 571–591. [https://doi.org/10.1175/1520-0442\(2003\)016<0571:BPOASF>2.0.CO;2](https://doi.org/10.1175/1520-0442(2003)016<0571:BPOASF>2.0.CO;2)
- Frankignoul, C., Czaja, A., & L'Heveder, B. (1998). Air-sea feedback in the North Atlantic and surface boundary conditions for ocean models. *Journal of Climate*, 11(9), 2310–2324. [https://doi.org/10.1175/1520-0442\(1998\)011<2310:ASFITN>2.0.CO;2](https://doi.org/10.1175/1520-0442(1998)011<2310:ASFITN>2.0.CO;2)
- Frankignoul, C., Gastineau, G., & Kwon, Y.-O. (2017). Estimation of the SST response to anthropogenic and external forcing and its impact on the Atlantic Multidecadal Oscillation and the Pacific Decadal Oscillation. *Journal of Climate*, 30(24), 9871–9895. <https://doi.org/10.1175/JCLI-D-17-0009.1>
- Frankignoul, C., & Hasselmann, K. (1977). Stochastic climate models, Part II Application to sea-surface temperature anomalies and thermocline variability. *Tellus*, 29(4), 289–305. <https://doi.org/10.3402/tellusa.v29i4.11362>
- Frankignoul, C., & Kestenare, E. (2002). The surface heat flux feedback. Part I: Estimates from observations in the Atlantic and the North Pacific. *Climate Dynamics*, 19(8), 633–647. <https://doi.org/10.1007/s00382-002-0252-x>
- Frenger, I., Gruber, N., Knutti, R., & Münnich, M. (2013). Imprint of Southern Ocean eddies on winds, clouds and rainfall. *Nature Geoscience*, 6(8), 608–612. <https://doi.org/10.1038/NNGEO1863>
- Gaube, P., Chelton, D., Samelson, R. M., Schlax, M. G., & O'Neill, L. W. (2015). Satellite observations of mesoscale eddy-induced Ekman pumping. *Journal of Physical Oceanography*, 45(1), 104–132. <https://doi.org/10.1175/JPO-D-14-0032.1>
- Gent, P. R., & McWilliams, J. C. (1990). Isopycnal mixing in ocean circulation models. *Journal of Physical Oceanography*, 20(1), 150–155. [https://doi.org/10.1175/1520-0485\(1990\)020<0150:IMIOCM>2.0.CO;2](https://doi.org/10.1175/1520-0485(1990)020<0150:IMIOCM>2.0.CO;2)
- Hall, A., & Manabe, S. (1997). Can local linear stochastic theory explain sea surface temperature and salinity variability? *Climate Dynamics*, 13(3), 167–180. <https://doi.org/10.1007/s003820050158>
- Hasselmann, K. (1976). Stochastic climate models Part I. Theory. *Tellus*, 28(6), 473–485. <https://doi.org/10.1111/j.2153-3490.1976.tb00696.x>
- Hunke, E. C., & Lipscomb, W. H. (2010). *CICE: The Los Alamos sea ice model documentation and software user's manual version 4.1*. (Vol. 87545, p. 76). Los Alamos as Alamos National Laboratory Tech.
- Joh, Y., Di Lorenzo, E., Siqueira, L., & Kirtman, B. P. (2021). Enhanced interactions of Kuroshio extension with tropical Pacific in a changing climate. *Scientific Reports*, 11(1), 6247. <https://doi.org/10.1038/s41598-021-85582-y>
- Kalnay, E., Kanamitsu, M., Kistler, R., Collins, W., Deaven, D., Gandin, L., et al. (1996). The NCEP/NCAR 40-year reanalysis Project. *Bulletin of the American Meteorological Society*, 77(3), 437–471. [https://doi.org/10.1175/1520-0477\(1996\)077<0437:TNYRP>2.0.CO;2](https://doi.org/10.1175/1520-0477(1996)077<0437:TNYRP>2.0.CO;2)
- Kanamitsu, M., Ebisuzaki, W., Woollen, J., Yang, S.-K., Hnilo, J. J., Fiorino, M., & Potter, G. L. (2002). NCEP-DOE AMIP-II reanalysis (R-2). *Bulletin of the American Meteorological Society*, 83(11), 1631–1643. <https://doi.org/10.1175/BAMS-83-11-1631>
- Kirtman, B. P., Bitz, C., Bryan, F., Collins, W., Dennis, J., Hearn, N., et al. (2012). Impact of ocean model resolution on CCSM climate simulations. *Climate Dynamics*, 39(6), 1303–1328. <https://doi.org/10.1007/s00382-012-1500-3>
- Kirtman, B. P., Perlin, N., & Siqueira, L. (2017). Ocean eddies and climate predictability. *Chaos*, 27(12), 126902. <https://doi.org/10.1063/1.4990034>
- Koszalka, I., LaCasce, J. H., Andersson, M., Orvik, K. A., & Mauritzen, C. (2011). Surface circulation in the Nordic Seas from clustered drifters. *Deep-Sea Research I*, 58(4), 468–485. <https://doi.org/10.1016/j.dsr.2011.01.007>
- Kubota, M., Iwasaka, N., Kizu, S., Konda, M., & Kutsuwada, K. (2002). Japanese ocean flux data sets with use of remote sensing observations (J-OFURO). *Journal of Oceanography*, 58(1), 213–225. <https://doi.org/10.1023/A:1015845321836>
- Large, W. G., & Yeager, S. G. (2004). Diurnal to decadal global forcing for ocean and sea-ice models: The data sets and flux climatologies. *NCAR technical note NCAR/TN-460+STR*. <https://doi.org/10.5065/D6KK98Q6>
- Larson, S. M., Vimont, D. J., Clement, A. C., & Kirtman, B. P. (2018). How momentum coupling affects SST variance and large-scale Pacific climate variability in CESM. *Journal of Climate*, 31(7), 2927–2944. <https://doi.org/10.1175/JCLI-D-17-0645.1>
- Laurindo, L. C., Siqueira, L., Mariano, A. J., & Kirtman, B. P. (2019). Cross-spectral analysis of the SST/10-m wind speed coupling resolved by satellite products and climate model simulations. *Climate Dynamics*, 52(9), 5071–5098. <https://doi.org/10.1007/s00382-018-4434-6>

- Lawrence, D. M., Oleson, K. W., Flanner, M. G., Thornton, P. E., Swenson, S. C., Lawrence, P. J., et al. (2011). Parameterization improvements and functional and structural advances in version 4 of the community Land model. *Journal of Advances in Modeling Earth Systems*, 3(1), M03001. <https://doi.org/10.1029/2011MS000045>
- Lee, D. E., Liu, Z., & Liu, Y. (2008). Beyond thermal interaction between ocean and atmosphere: On the extratropical climate variability due to the wind-induced SST. *Journal of Climate*, 21(10), 2001–2018. <https://doi.org/10.1175/2007JCLI1532.1>
- Lindborg, E. (2006). The energy cascade in a strongly stratified fluid. *Journal of Fluid Mechanics*, 550(-1), 207–242. <https://doi.org/10.1017/S0022112005008128>
- Ma, X., Chang, P., Saravanan, R., Montuoro, R., Hsieh, J.-S., Wu, D., et al. (2015). Distant influence of Kuroshio eddies on North Pacific weather patterns? *Scientific Reports*, 5(1), 17785. <https://doi.org/10.1038/srep17785>
- Ma, X., Chang, P., Saravanan, R., Montuoro, R., Nakamura, H., Wu, D., et al. (2017). Importance of resolving Kuroshio front and eddy influence in simulating the North Pacific storm track. *Journal of Climate*, 30(5), 1861–1880. <https://doi.org/10.1175/JCLI-D-16-0154.1>
- Ma, X., Jing, Z., Chang, P., Liu, X., Montuoro, R., Small, R. J., et al. (2016). Western boundary currents regulated by interaction between ocean eddies and the atmosphere. *Nature*, 535(7613), 533–537. <https://doi.org/10.1038/nature18640>
- Mahajan, S., Saravanan, R., & Chang, P. (2009). The role of the wind-evaporation-sea surface temperature (WES) feedback in air–sea coupled tropical variability. *Atmospheric Research*, 94(1), 19–36. <https://doi.org/10.1016/j.atmosres.2008.09.017>
- Mariano, A. J., Ryan, E. H., Huntley, H. S., Laurindo, L., Coelho, E., Griffa, A., et al. (2016). Statistical properties of the surface velocity field in the northern Gulf of Mexico sampled by GLAD drifters. *Journal of Geophysical Research: Oceans*, 121(7), 5193–5216. <https://doi.org/10.1002/2015JC011569>
- Martin, P. E., Arbic, B. K., & Hogg, A. M. (2021). Drivers of atmospheric and oceanic surface temperature variance: A frequency domain approach. *Journal of Climate*, 34(10), 3975–3990. <https://doi.org/10.1175/JCLI-D-20-0557.1>
- Martínez-Villalobos, C., Newman, M., Vimont, D. J., Penland, C., & David Neelin, J. (2019). Observed el niño-la niña asymmetry in a linear model. *Geophysical Research Letters*, 46(16), 9909–9919. <https://doi.org/10.1029/2019GL082922>
- Meehl, G. A., Yang, D., Arblaster, J. M., Bates, S. C., Rosenbloom, N., Neale, R., et al. (2019). Effects of model resolution, physics, and coupling on southern hemisphere storm tracks in CESM1.3. *Geophysical Research Letters*, 46(21), 12408–12416. <https://doi.org/10.1029/2019GL084057>
- Minobe, S., Kuwano-Yoshida, A., Komori, N., Xie, S.-P., & Small, R. J. (2008). Influence of the Gulf Stream on the troposphere. *Nature*, 452(7184), 206–209. <https://doi.org/10.1038/nature06690>
- Nastrom, G. D., & Gage, K. S. (1985). A climatology of atmospheric wavenumber spectra of wind and temperature observed by commercial aircraft. *Journal of the Atmospheric Sciences*, 42(9), 950–960. [https://doi.org/10.1175/1520-0469\(1985\)042<0950:ACOWS>2.0.CO;2](https://doi.org/10.1175/1520-0469(1985)042<0950:ACOWS>2.0.CO;2)
- Neale, R. B., Gettelman, A., Park, S., Chen, C.-C., Lauritzen, P. H., Williamson, D. L., et al. (2012). *Description of the NCAR community atmosphere model (CAM 5.0)* (p. 289). NCAR TECHNICAL NOTE NCAR/TN-486+STR.
- O'Brien, R. C., Cipollini, P., & Blundell, J. R. (2013). Manifestation of oceanic Rossby waves in long-term multiparametric satellite datasets. *Remote Sensing of Environment*, 129, 111–121. <https://doi.org/10.1016/j.rse.2012.10.024>
- Okumura, Y., Xie, S.-P., Numaguti, A., & Tanimoto, Y. (2001). Tropical Atlantic air-sea interaction and its influence on the NAO. *Geophysical Research Letters*, 28(8), 1507–1510. <https://doi.org/10.1029/2000GL012565>
- O'Neill, L. W., Chelton, D. B., & Esbensen, S. K. (2010). The effects of SST-induced surface wind speed and direction gradients on midlatitude surface vorticity and divergence. *Journal of Climate*, 23(2), 255–281. <https://doi.org/10.1175/2009JCLI2613.1>
- O'Reilly, C. H., Huber, M., Woollings, T., & Zanna, L. (2016). The signature of low-frequency oceanic forcing in the Atlantic Multidecadal Oscillation. *Geophysical Research Letters*, 43(6), 2810–2818. <https://doi.org/10.1002/2016GL067925>
- Park, S., Deser, C., & Alexander, M. A. (2005). Estimation of the surface heat flux response to sea surface temperature anomalies over the global oceans. *Journal of Climate*, 18(21), 4582–4599. <https://doi.org/10.1175/jcli3521.1>
- Park, S., Deser, C., & Alexander, M. A. (2006). The impact of cloud radiative feedback, remote ENSO forcing, and entrainment on the persistence of north Pacific sea surface temperature anomalies. *Journal of Climate*, 19(23), 6243–6261. <https://doi.org/10.1175/jcli3957.1> <https://journals.ametsoc.org/view/journals/clim/19/23/jcli3957.1.xml>
- Patrizio, C. R., & Thompson, D. W. J. (2021). Quantifying the role of ocean dynamics in ocean mixed layer temperature variability. *Journal of Climate*, 34(7), 2567–2589. <https://doi.org/10.1175/JCLI-D-20-0476.1>
- Patrizio, C. R., & Thompson, D. W. J. (2022). Understanding the role of ocean dynamics in midlatitude sea surface temperature variability using a simple climate model. *Journal of Climate*, 35(11), 3313–3333. (Published online ahead of print 2022. <https://doi.org/10.1175/JCLI-D-21-0184.1>)
- Peng, S., Qian, Y.-K., Lumpkin, R., Li, P., Wang, D., & Du, Y. (2015). Characteristics of the near-surface currents in the Indian ocean as deduced from satellite-tracked surface drifters. Part II: Lagrangian statistics. *Journal of Physical Oceanography*, 45(2), 459–477. <https://doi.org/10.1175/JPO-D-14-0049.1>
- Polito, P. S., & Sato, O. T. (2015). Do eddies ride on Rossby waves? *Journal of Geophysical Research: Oceans*, 120(8), 5417–5435. <https://doi.org/10.1002/2015JC010737>
- Proistosescu, C., Donohoe, A., Armour, K. C., Roe, G. H., Stuecker, M. F., & Bitz, C. M. (2018). Radiative feedbacks from stochastic variability in surface temperature and radiative imbalance. *Geophysical Research Letters*, 45(10), 5082–5094. <https://doi.org/10.1029/2018GL077678>
- Putrasahan, D. A., Kamenkovich, I., Le Hénaff, M., & Kirtman, B. P. (2017). Importance of ocean mesoscale variability for air-sea interactions in the Gulf of Mexico. *Geophysical Research Letters*, 44(12), 6352–6362. <https://doi.org/10.1002/2017GL072884>
- Putrasahan, D. A., Miller, A., & Seo, H. (2013). Isolating mesoscale coupled ocean–atmosphere interactions in the Kuroshio Extension region. *Dynamics of Atmospheres and Oceans*, 63, 60–78. <https://doi.org/10.1016/j.dynatmoce.2013.04.001>
- Roberts, M. J., Hewitt, H. T., Hyder, P., Ferreira, D., Josey, S. A., Mizielinski, M., & Shelly, A. (2016). Impact of ocean resolution on coupled air-sea fluxes and large-scale climate. *Geophysical Research Letters*, 43(19), 10430–10438. <https://doi.org/10.1002/2016GL070559>
- Sérazin, G., Jaymond, A., Leroux, S., Penduff, T., Bessières, L., Llovel, W., et al. (2017). A global probabilistic study of the ocean heat content low-frequency variability: Atmospheric forcing versus oceanic chaos. *Geophysical Research Letters*, 44(11), 5580–5589. <https://doi.org/10.1002/2017GL073026>
- Sérazin, G., Penduff, T., Barnier, B., Molines, J.-M., Arbic, B. K., Müller, M., & Terray, L. (2018). Inverse cascades of kinetic energy as a source of intrinsic variability: A global OGCM study. *Journal of Physical Oceanography*, 48(6), 1385–1408. <https://doi.org/10.1175/JPO-D-17-0136.1>
- Sérazin, G., Penduff, T., Grégorio, S., Barnier, B., Molines, J.-M., & Terray, L. (2015). Intrinsic variability of sea level from global ocean simulations: Spatiotemporal scale. *Journal of Climate*, 28(10), 4279–4292. <https://doi.org/10.1175/JCLI-D-14-00554.1>
- Siqueira, L., & Kirtman, B. (2016). Atlantic near-term climate variability and the role of a resolved Gulf Stream. *Geophysical Research Letters*, 43(8), 3964–3972. <https://doi.org/10.1002/2016GL068694>
- Siqueira, L., Kirtman, B., & Laurindo, L. C. (2021). Forecasting remote atmospheric responses to decadal Kuroshio stability transitions. *Journal of Climate*, 34(1), 379–395. <https://doi.org/10.1175/JCLI-D-20-0139.1>

- Small, R. J., Bryan, F. O., Bishop, S. P., Larson, S., & Tomas, R. A. (2020). What drives upper-ocean temperature variability in coupled climate models and observations. *Journal of Climate*, 33(2), 577–596. <https://doi.org/10.1175/JCLI-D-19-0295.1>
- Small, R. J., Bryan, F. O., Bishop, S. P., & Tomas, R. A. (2019). Air–sea turbulent heat fluxes in climate models and observational analyses: What drives their variability? *Journal of Climate*, 32(8), 2397–2421. <https://doi.org/10.1175/JCLI-D-18-0576.1>
- Small, R. J., de Szoeke, S. P., Xie, S.-P., O’Neill, L., Seo, H., Song, Q., et al. (2008). Air–sea interaction over ocean fronts and eddies. *Dynamics of Atmospheres and Oceans*, 45(3–4), 274–319. <https://doi.org/10.1016/j.dynatmoce.2008.01.001>
- Smirnov, D., Newman, M., & Alexander, M. A. (2014). Investigating the role of ocean–atmosphere coupling in the North Pacific Ocean. *Journal of Climate*, 27(2), 592–606. <https://doi.org/10.1175/JCLI-D-13-00123.1>
- Smirnov, D., Newman, M., Alexander, M. A., Kwon, Y.-O., & Frankignoul, C. (2015). Investigating the local atmospheric response to a realistic shift in the Oyashio sea surface temperature front. *Journal of Climate*, 28(3), 1126–1147. <https://doi.org/10.1175/JCLI-D-14-00285.1>
- Smith, R., Jones, P., Briegleb, B., Bryan, F., Danabasoglu, G., Dennis, J., et al. (2010). *The Parallel Ocean Program (POP) reference manual* (p. 141). Los Alamos National Laboratory Tech. Rep. LAUR-10-01853.
- Spencer, R. W., & Braswell, W. D. (2010). On the diagnosis of radiative feedback in the presence of unknown radiative forcing. *Journal of Geophysical Research*, 115(D16), D16109. <https://doi.org/10.1029/2009JD013371>
- Sun, X., & Wu, R. (2021). Seasonality and time scale dependence of the relationship between turbulent surface heat flux and SST. *Journal of Climate*, 56(9–10), 3173–3186. <https://doi.org/10.1007/s00382-021-05631-0>
- Sura, P., & Newman, M. (2008). The impact of rapid wind variability upon air–sea thermal coupling. *Journal of Climate*, 21(4), 621–637. <https://doi.org/10.1175/2007JCLI1708.1>
- Sura, P., Newman, M., & Alexander, M. A. (2006). Daily to decadal sea surface temperature variability driven by state-dependent stochastic heat fluxes. *Journal of Physical Oceanography*, 36(10), 1940–1958. <https://doi.org/10.1175/JPO2948.1>
- Sura, P., & Sardeshmukh, P. D. (2009). A global view of air–sea thermal coupling and related non-Gaussian SST variability. *Atmospheric Research*, 94(1), 140–149. <https://doi.org/10.1016/j.atmosres.2008.08.008>
- Tomita, H., Hihara, T., Kako, S., Kubota, M., & Kutsuwada, K. (2019). An introduction to J-OFURO3, a third-generation Japanese ocean flux data set using remote-sensing observations. *Journal of Oceanography*, 75(2), 71–194. <https://doi.org/10.1007/s10872-018-0493-x>
- Tulloch, R., & Smith, K. S. (2009). Quasigeostrophic turbulence with explicit surface dynamics: Application to the atmospheric energy spectrum. *Journal of the Atmospheric Sciences*, 66(2), 450–467. <https://doi.org/10.1175/2008JAS2653.1>
- Villas Bôas, A. B., Sato, O. T., Chaigneau, A., & Castelão, G. P. (2015). The signature of mesoscale eddies on the air–sea turbulent heat fluxes in the South Atlantic Ocean. *Geophysical Research Letters*, 42(6), 1856–1862. <https://doi.org/10.1002/2015GL063105>
- von Storch, J.-S. (2000). Signatures of air–sea interactions in a coupled atmosphere–ocean GCM. *Journal of Climate*, 13(19), 3361–3379. [https://doi.org/10.1175/1520-0442\(2000\)013<3361:SOASII>2.0.CO;2](https://doi.org/10.1175/1520-0442(2000)013<3361:SOASII>2.0.CO;2)
- Wills, S. M., & Thompson, D. W. J. (2018). On the observed relationships between wintertime variability in Kuroshio–Oyashio extension sea surface temperatures and the atmospheric circulation over the North Pacific. *Journal of Climate*, 31(12), 4669–4681. <https://doi.org/10.1175/JCLI-D-17-0343.1>
- Wills, S. M., Thompson, D. W. J., & Ciasto, L. M. (2016). On the observed relationships between variability in Gulf Stream sea surface temperatures and the atmospheric circulation over the North Atlantic. *Journal of Climate*, 29(10), 3719–3730. <https://doi.org/10.1175/JCLI-D-15-0820.1>
- Wu, R., Kirtman, B. P., & Pegion, K. (2006). Local air–sea relationship in observations and model simulations. *Journal of Climate*, 19, 4914–4932. <https://doi.org/10.1175/JCLI3904.1>
- Xie, S.-P. (2004). Satellite observations of cool ocean–atmosphere interaction. *Bulletin of the American Meteorological Society*, 85(2), 195–208. <https://doi.org/10.1175/BAMS-85-2-195>
- Yook, S., Thompson, D. W. J., Sun, L., & Patrizio, C. (2022). The simulated atmospheric response to Western North Pacific sea surface temperature anomalies. *Journal of Climate*, 35(11), 3335–3352. <https://doi.org/10.1175/JCLI-D-21-0371.1>
- Zhang, S., Fu, H., Wu, L., Li, Y., Wang, H., Zeng, Y., et al. (2020). Optimizing high-resolution community Earth system model on a heterogeneous many-core supercomputing platform. *Geoscientific Model Development*, 13(10), 4809–4829. <https://doi.org/10.5194/gmd-13-4809-2020>
- Zhurbas, V., Lyzhkov, D., & Kuzmina, N. (2014). Drifter-derived estimates of lateral eddy diffusivity in the World Ocean with emphasis on the Indian Ocean and problems of parameterisation. *Deep-Sea Research I*, 83, 1–11. <https://doi.org/10.1016/j.dsr.2013.09.001>